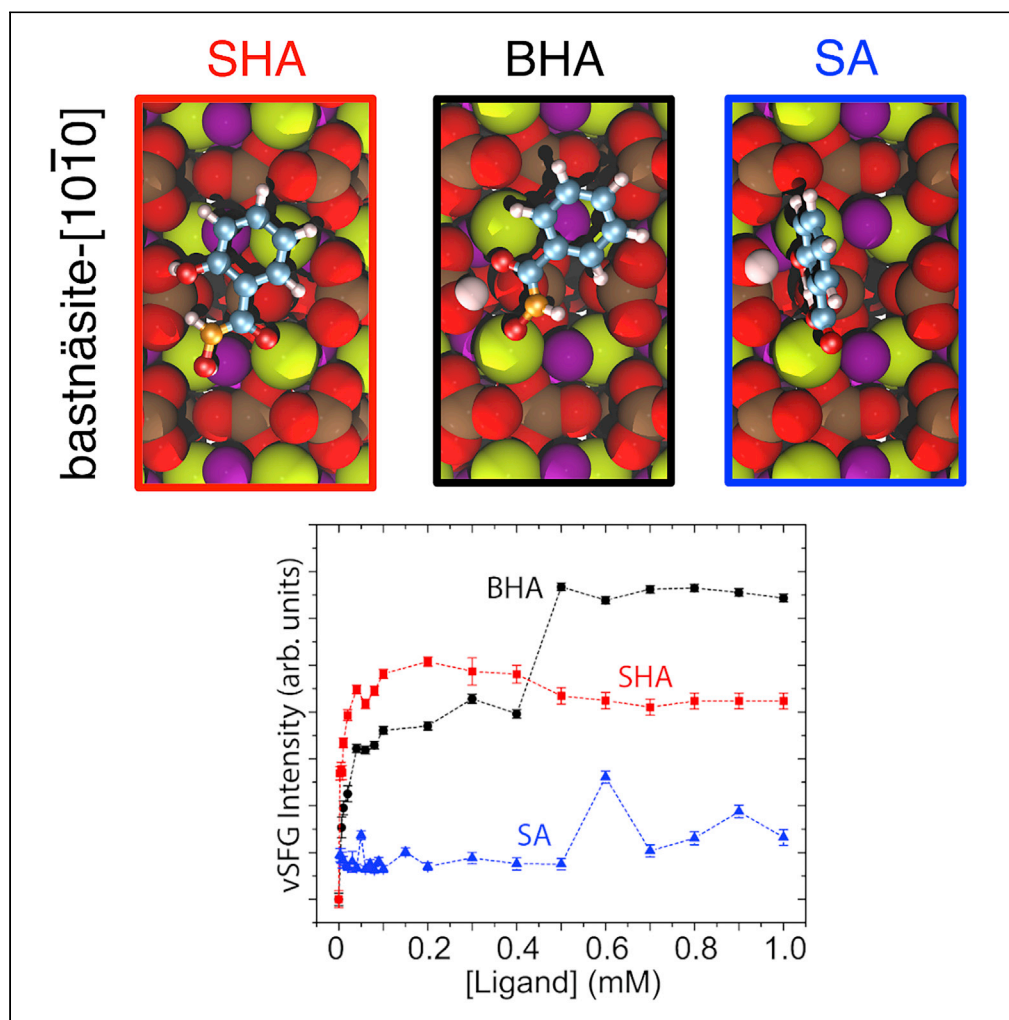Article

A Molecular-Scale Approach to Rare-Earth Beneficiation: Thinking Small to Avoid Large Losses

Robert C. Chapleski, Jr., Azhad U. Chowdhury, Anna K. Wanhala, ..., Corby G. Anderson, Benjamin Doughty, Vyacheslav S. Bryantsev

doughtybl@ornl.gov (B.D.)
bryantsevv@ornl.gov (V.S.B.)

HIGHLIGHTS

Salicylhydroxamic acid (SHA) is an effective collector for flotation of bastnäsite

DFT calculations show that the phenol group anchors SHA flat to bastnäsite surface

Spectroscopic results suggest SHA multilayers on bastnäsite at high coverage

This peculiar adsorption explains efficacy of SHA in bastnäsite flotation from ores

iScience

Article

A Molecular-Scale Approach to Rare-Earth Beneficiation: Thinking Small to Avoid Large Losses

Robert C. Chapleski, Jr.,[1] Azhad U. Chowdhury,[1] Anna K. Wanhala,[1] Vera Bocharova,[1] Santanu Roy,[1] Philip C. Keller,[2] Dylan Everly,[2] Santa Jansone-Popova,[1] Alexander Kisliuk,[1] Robert L. Sacci,[1] Andrew G. Stack,[1] Corby G. Anderson,[2] Benjamin Doughty,[1,*] and Vyacheslav S. Bryantsev[1,3,*]

SUMMARY

Separating rare-earth-element-rich minerals from unwanted gangue in mined ores relies on selective binding of collector molecules at the interface to facilitate froth flotation. Salicylhydroxamic acid (SHA) exhibits enhanced selectivity for bastnäsite over calcite in microflotation experiments. Through a multifaceted approach, leveraging density functional theory calculations, and advanced spectroscopic methods, we provide molecular-level mechanistic insight to this selectivity. The hydroxamic acid moiety introduces strong interactions at metal-atom surface sites and hinders subsurface-cation stabilization at vacancy-defect sites, in calcite especially. Resulting from hydrogen-bond-induced interactions, SHA lies flat on the bastnäsite surface and shows a tendency for multilayer formation at high coverages. In this conformation, SHA complexation with bastnäsite metal ions is stabilized, leading to advanced flotation performance. In contrast, SHA lies perpendicular to the calcite surface due to a difference in cationic spacing. We anticipate that these insights will motivate rational design and selection of future collector molecules for enhanced ore beneficiation.

INTRODUCTION

Rare-earth elements (REEs) have widespread applications, ranging from catalysts in automobiles and petroleum refining to polishing media, magnets in computer equipment and wind turbines, batteries, phosphors in lighting, and medical diagnostic equipment (Eggert et al., 2016; Ganguli and Cook, 2018; Jordens et al., 2013; Tunsu et al., 2015). These "rare" elements are so named for the paucity of mineral deposits containing them in mineable quantities, despite their fair abundance in the Earth's crust (Eggert et al., 2016). The existence of so few economically viable reserves, coupled with a year-over-year increase in demand (Eggert et al., 2016), highlights the need for more efficient strategies for extracting REEs from mined ores.

REEs are subclassified into two groups: the light rare-earth elements (LREEs), La to Eu, and the heavy rare-earth elements (HREEs), Gd to Lu and Y (Krishnamurthy and Gupta, 2016). The largest mineral sources of LREEs are bastnäsite deposits in Bayan Obo, China, and Mountain Pass, California, USA (Castor, 2008; Drew et al., 1990; Eggert et al., 2016; Kynicky et al., 2012; Mariano and Mariano, 2012; Yang et al., 2011). Bastnäsite is a fluoro-carbonate mineral with the chemical formula $MFCO_3$ (M = Ce (~50%), La (~30%), and other LREEs) (Eggert et al., 2016; Long et al., 2010; Weng et al., 2015). Obtaining REEs from these mineral sources first requires beneficiation, or the separation of bastnäsite from unwanted gangue materials in the ore. Bastnäsite beneficiation is currently achieved by means of froth flotation (Cui and Anderson, 2017a; Liu et al., 2019). In this process, a slurry of ore is prepared, containing a collector molecule that selectively adsorbs to the bastnäsite particles, increasing their hydrophobicity. Air is then bubbled through the slurry, and the hydrophobic bastnäsite adheres to the bubbles, which float to the top of the flotation cell and are skimmed off for further processing. The grade of beneficiated ore thus relies on selective adsorption of the collector onto the surfaces of bastnäsite. Separation of bastnäsite from calcite, the most abundant gangue mineral (Pradip and Fuerstenau, 2013), is particularly difficult, because both of these salt-type minerals (Gallios and Matis, 1992) include carbonate anions as integral components of their functional units.
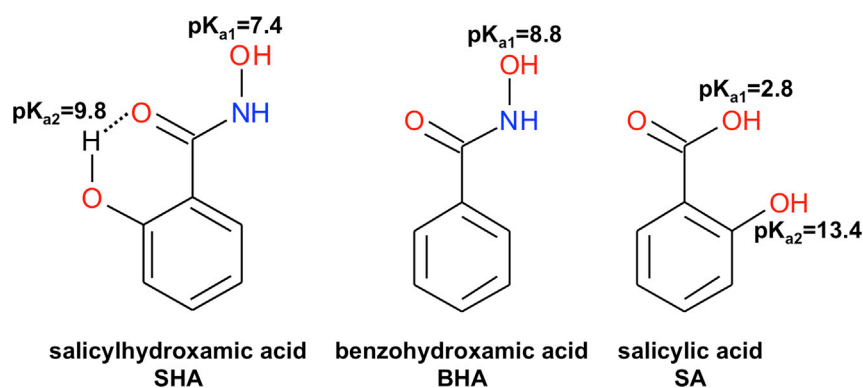
[1]Chemical Sciences Division, Oak Ridge National Laboratory, 1 Bethel Valley Road, Oak Ridge, TN 27831, USA

[2]Kroll Institute for Extractive Metallurgy, Colorado School of Mines, Golden, CO 80401, USA

[3]Lead Contact

*Correspondence: doughtybl@ornl.gov (B.D.), bryantsevv@ornl.gov (V.S.B.) https://doi.org/10.1016/j.isci.2020.101435

Scheme 1. Skeletal Structures and pK$_a$ Values for the Three Collector Ligands Investigated in This Work
SHA and BHA both exhibit the C(=O)-NR-OH hydroxamic acid moiety.

Beginning with initial reports in the 1960s of their flotability (Fuerstenau; Peterson, 1969), hydroxamic acid compounds have shown selectivity for REE minerals (Assis et al., 1996; Cui and Anderson, 2017b; Liu et al., 2019; Nagaraj, 1992; Pradip and Fuerstenau, 2013; Wanhala et al., 2019; Yoon and Hilderbrand, 1986; Zhang et al., 2014). Nonetheless, beneficiation with hydroxamic acid results in the recovery of only 60%–72% REE from the primary ore, with the rest lost in the gangue (Nagaraj and Farinato, 2016; Talens Peiró; Villalba Méndez, 2013). This loss highlights the need for advanced collector ligands with enhanced selectivity for bastnäsite over gangue materials.

Since the inception of collection with hydroxamic acid ligands, extensive progress has been made in describing the interactions between the hydroxamic acid group (Scheme 1, with pKa values from Humbert et al., 1998; Khalil et al., 2007) and metal ions in terms of chemisorption on REE mineral surfaces and weaker adsorption on gangue (Anderson, 2015; Cao et al., 2019; Marion et al., 2020; Nagaraj, 2018; Pradip and Fuerstenau, 1983, 1985; Xiong et al., 2020). Typically, chemisorption results in chelation, forming a five-membered ring through interactions between both hydroxamic oxygen atoms and a surface cation (Nagaraj, 2018; Ren et al., 1997). Electronic effects of the hydroxamic acid moiety in selective adsorption have also been discussed thoroughly (Nagaraj, 2018).

New hydroxamic acid collector ligands are traditionally selected through a trial-and-error approach, guided by empirical trends and observations of flotation in other materials. Studies have begun to extend a molecular-level approach beyond the hydroxamic acid moiety, toward a comprehensive understanding of adsorption in terms of specific structural interactions among functional groups in the collector, water molecules, and atoms in the mineral surface. This detail-oriented perspective, which has been employed for other metal- and mineral-ligand systems (Frey et al., 2000; Rio-Echevarria et al., 2008; Waterson et al., 2016), can lead to the rational design of future collector ligands.

Such an approach entails the *molecular recognition of surfaces*, wherein structural features of a ligand molecule are aligned with those of the mineral surface, leading favorably to adsorption. Motivated by bio-mineralization phenomena resulting in the natural production of materials such as oyster shells, ivory, and pearls in living creatures as a result of structural similarities in organic polymers and inorganic minerals, Pradip and co-workers have pioneered a description of collector selectivity and flotation efficacy in terms of differences in ligand recognition across mineral surfaces (Elam, 2014; Pradip, 1992; Pradip and Rai, 2003; Pradip et al., 2002). Previous work has enlisted coverage-dependent isotherms to describe the orientation of ligands bound to a surface (Cases and Villieras, 1992). Investigations of the molecular recognition of surfaces extend these approaches by enlisting computational and spectroscopic methods, allowing us to "see" the adsorption state of molecules on the surface.

Joint spectroscopic-computational studies have recently begun to reveal adsorption structures and energies on bastnäsite surfaces (Espiritu et al., 2018). Wanhala et al., for instance, explored the mechanisms of adsorption of octyl hydroxamic acid to bastnäsite as a function of hydroxamic acid coverage (Wanhala et al., 2019). Implementing both attenuated total reflection-Fourier transform infrared (ATR-FTIR) and vibrational sum frequency generation (vSFG) spectroscopies, along with density functional theory (DFT),

	Grade		Recovery	
	REO (%)	REO/CaO	REO (%)	REO/CaO
Ore	7.7	0.5	–	–
Salicylhydroxamic acid (SHA)	33.4	2.5	66.6	5.5
Benzohydroxamic acid (BHA)	22.5	1.9	57.0	4.7
Salicylic acid (SA)	7.3	0.8	50.5	1.8

Table 1. Results of Microflotation Experiments, Reported in Terms of Rare-Earth Oxide (REO) and Calcium Oxide (CaO) Content

this work revealed coverage-dependent ligand binding and highlighted the role of the long alkyl chain in adsorption.

Aromatic hydroxamic ligands have shown recent promise for bastnäsite flotation (Everly, 2017). Studies employing these collectors have optimized the conditions for flotation and describe the adsorption of some of these ligands onto the surface (Cao et al., 2018; Jordens et al., 2014, 2016; Li et al., 2018; Marion et al., 2020; Xia et al., 2014; Yang et al., 2017; Yu et al., 2020). Here, we provide mechanistic insight into the adsorption of one aromatic ligand, salicylhydroxamic acid (N,2-dihydroxybenzamide, SHA), through a series of investigations designed to relate structure to adsorption selectivity. SHA has shown good performance for LREE recovery (Xia et al., 2014), and previous work employing flotation and contact-angle studies reveals increased bastnäsite hydrophobicity following treatment with SHA, contributing to its flotability (Cao et al., 2018; Xiong et al., 2020). Recent work has compared the optimal conditions for SHA flotation of bastnäsite with those of gangue minerals, including calcite, using spectroscopic, microflotation, and zeta-potential measurements (Xiong et al., 2020). Importantly, this study revealed stronger chemisorptive binding of SHA to bastnäsite and weaker physisorption to gangue minerals.

In the present work, a combined approach that enlists DFT, along with Raman, ATR-FTIR, and vSFG spectroscopies, affords a comprehensive molecular-level description of adsorption. Results of parallel studies on the adsorption of SHA, benzohydroxamic acid (N-hydroxybenzamide, BHA), and salicylic acid (2-hydroxybenzoic acid, SA) ligands onto bastnäsite demonstrate the roles of functional groups important to beneficiation by flotation with SHA. In this manner, we are able to conceptually deconstruct the ligand into a sum of functionalities in order to relate the structure of the ligand to surface recognition. The structure of SHA, shown in Scheme 1 along with the other two ligands, consists of a benzene ring with *ortho*-hydroxamic acid and phenolic moieties. BHA has a similar structure, lacking only the phenol group. By comparing DFT and experimental results for SHA and BHA, new insight into the role of the *ortho*-phenol group in the adsorption of SHA is elucidated. Similarly, SA differs from SHA through the substitution of the hydroxamic acid group for a carboxylic acid group. A comparison of results using these substituted ligands provides insight into the role of the hydroxamic acid moiety in the recognition of bastnäsite and calcite surfaces, as well as on the beneficiative properties of SHA.

With limited mineable rare-earth resources, strategies must be developed that will enhance the availability of these critical materials. We anticipate that detailed insights such as those gained from our systematic, molecular-scale approach will influence the design of compounds that can more effectively separate rare-earth-containing mineral compounds from gangue.

RESULTS

Microflotation Experiments

The results of microflotation experiments for the three ligands on bastnäsite are given in Table 1. The beneficiation potential of the three ligands decreases in the order SHA > BHA > SA, as reflected by both sample grade and total rare-earth oxide (REO) recovery. From an ore sample containing 7.7% rare-earth oxide by weight, flotation with SHA results in the greatest total recovery of REO (66.6%), with an increase in grade to 33.4% REO. This corresponds to 5.5 times as much REO recovered as calcium oxides (CaO), with a concentration of REO 2.5 times that of CaO in the recovered froth, indicating selectivity of SHA for bastnäsite over calcite. This result is in good agreement with recent microflotation studies of bastnäsite ores with SHA

Mineral	Salicylhydroxamic Acid (SHA)	Benzohydroxamic Acid (BHA)	Salicylic Acid (SA)
Bastnäsite-[10$\bar{1}$0]	−48.9	−50.1	−32.5
Calcite-[10$\bar{1}$4]	−59.2	−19.2	−43.2

Table 2. Collector Adsorption Energies (kJ/mol) on Bastnäsite-[10$\bar{1}$0] and Calcite-[10$\bar{1}$4] Surfaces with Dipole and Solvent Corrections Included

(Xiong et al., 2020). BHA also shows some capability as a collector, increasing the grade to 22.5% REO by weight, and recovering 57.0% of the REO from the original ore. BHA selectivity for bastnäsite is also noted, recovering 4.7 times as much REO as CaO from the ore. SA, which shows almost no selectivity for bastnäsite, yields microflotation froth with a composition resembling that of the starting ore.

Density Functional Theory Calculations

Periodic-DFT-calculated adsorption energies for SHA, BHA, and SA on bastnäsite-[10$\bar{1}$0], the most prevalent bastnäsite surface (Srinivasan et al., 2017; Srinivasan et al., 2016), with acidic protons proximal to the adsorbate, are provided in Table 2, and optimized structures are shown in Figure 1 and detailed in Figure S1 with interactions contributing to adsorption specified.

The optimized structures for SHA and BHA, which exhibit different binding modes on the bastnäsite surface, result in similar adsorption energies. In its most stable adsorption orientation, BHA binds in a bridging fashion to two surface Ce^{3+} cations via both hydroxamic acid oxygen atoms, as well as through a hydrogen bond donated by a protonated carbonate moiety to the carbonyl oxygen, resulting in an adsorption energy of −50.1 kJ/mol. Conversely, SHA adsorbs with an energy of −48.9 kJ/mol through a single monodentate interaction with surface Ce^{3+}, along with two hydrogen bonds with surface anionic groups. Previous work highlights the role of hydrogen bonding in SHA adsorption to mineral surfaces and describes a bidentate chelation binding mechanism between the hydroxamic acid moiety and the surface (Cao et al., 2019). In contrast, the lowest-energy structure for SHA on bastnäsite that we present in Figure 1 is 6.5 kJ/mol more stable than the complex in which SHA exhibits bidentate chelation, revealing in a surface-perpendicular orientation. (i.e., structure D in Figure S6).

Both BHA and SHA adsorb onto the surface with their aromatic ring moieties oriented essentially parallel to the surface plane. In SHA, the hydrogen bond afforded by the additional phenolic moiety anchors the ring to the surface, resulting in a more surface-parallel ring in SHA than in BHA (Figure S6).

SA, like BHA, shows adsorption to bastnäsite to two surface Ce^{3+} cations and a single hydrogen bonding interaction. Without the constraint of a bound hydroxamic group, the aromatic ring is now oriented more vertically with respect to the surface, implicating the binding configuration of the hydroxamic acid group in the orientation of the ring in SHA along the surface. Although the binding modes are similar, BHA adsorbs more strongly to the surface (E_{ads} = −50.1 kJ/mol) than does SA (E_{ads} = −32.5 kJ/mol), supporting the role of the hydroxamic acid moiety in strong SHA adsorption.

For insight into the selectivity of the three ligands for bastnäsite over calcite, we also explored the adsorption of SHA, BHA, and SA on the most stable calcite surface: [10$\bar{1}$4]. Adsorption energies of the lowest-energy configurations for each ligand-calcite system, with acidic protons near the site of adsorption, are provided in Table 2, and corresponding structures are shown in Figure 2 and detailed in Figure S2 with interactions contributing to adsorption specified.

BHA shows much weaker adsorption onto calcite (E_{ads} = −19.2 kJ/mol) than onto bastnäsite (E_{ads} = −50.1 kJ/mol), despite a similar adsorption mechanism including bridging interactions and a hydrogen bond. Closer cationic spacing on the calcite surface (d(Ca-Ca) = 4.03 and 4.99 Å) compared with the Ce-bastnäsite surface (d(Ce-Ce) = 4.78 and 7.07 Å) may allow for closer adsorption on the bastnäsite surface and potentially cause differing degrees of strain on the structure of the ligand upon adsorption. Previous work on bastnäsite-collector design highlights variations in cationic spacing in these surfaces (Srinivasan et al., 2017).
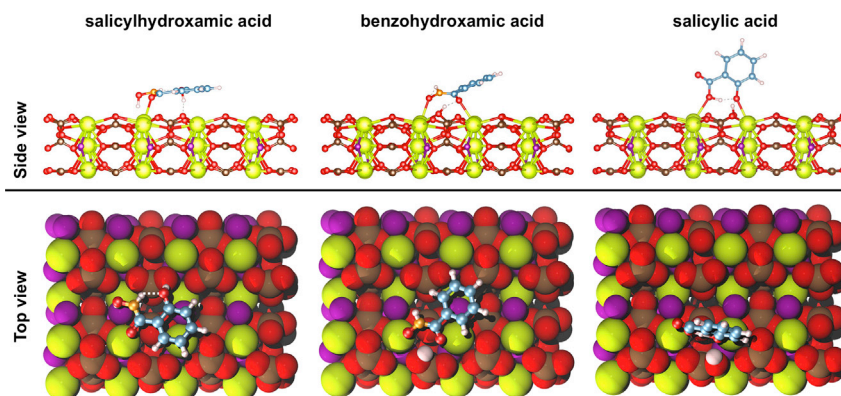
Figure 1. DFT Structures of the Most Stable Adsorption Configurations of Each Ligand on Bastnäsite-[10$\bar{1}$0]

Charge neutrality is maintained by having acidic proton(s) either on a ligand or surface-CO_3^{2-}/F^-. For clarity, side views show only the top three layers of bastnäsite slabs. Color scheme: Ce, light green; F, purple; N, orange; C, brown/cyan; O, red; H, white. See also Figure S1 for a detailed depiction of interactions contributing to adsorption.

SHA shows stronger adsorption (E_{ads} = −59.2 kJ/mol) on calcite than on bastnäsite (E_{ads} = −48.9 kJ/mol), resulting from a different adsorption mechanism. SHA binding to bastnäsite occurs through a single inter-action with a surface cation and two hydrogen bonds, whereas binding to calcite occurs through cationic interactions with all three oxygen atoms in SHA to different Ca^{2+} sites, and two hydrogen bonds with sur-face carbonate groups. In this case, closer cationic spacing in calcite leads to stronger adsorption through increased ligand-surface interaction. In order to facilitate an interaction between the phenolic oxygen and a nearby calcium ion, the aromatic ring moiety is now oriented more perpendicular to the surface. More-over, the adsorption structures of the hydroxamic acid moieties in BHA and SHA on calcite are essentially identical to one another, directly revealing the role of the phenolic moiety in SHA adsorption on calcite. In the absence of the phenol, the ring in BHA lies more flat on the surface while ligand adsorption becomes less energetically favorable by 40.0 kJ/mol.

SA on calcite also shows similar adsorption features to SHA, with a bridging structure involving two oxygens and surface Ca^{2+} cations. However, a third interaction with a surface cation is not possible with SA, as the carboxylic acid group, in the place of the larger hydroxamic acid group in SHA, is not able to reach to an additional surface cation (Figure S2). Thus, SA adsorbs more weakly onto calcite (E_{ads} = −43.2 kJ/mol) than SHA (E_{ads} = −59.2 kJ/mol). Nonetheless, SA adsorption on calcite is stronger than on bastnäsite (E_{ads} = −32.5 kJ/mol).

For DFT results discussed up to this point, we have considered only structures in which the acidic ligand protons are found either associated with or placed nearby on the surfaces of bastnäsite or calcite, in order to maintain charge neutrality in the system. We now turn to an alternative strategy, wherein SHA^{2-} and SA^{2-} replace, in their doubly deprotonated forms, a surface CO_3^{2-} anion (see Transparent Methods in Supplemental Information). This approach affords the advantage of considering adsorption at a single-site vacancy defect, providing initial insight into a nonideal-surface system such as those expected from mined ores.

Replacement of CO_3^{2-} by a ligand on the bastnäsite surface results in an energetic expense much less than that on the calcite surface (structures in Figures S3–S5, energies in Table S1). Despite showing more exten-sive SHA-surface interaction than on bastnäsite, the greater replacement energy on calcite is likely due to the inherent differences in structure between the [10$\bar{1}$0] surface of bastnäsite and the [10$\bar{1}$4] surface of calcite (Srinivasan et al., 2017). In the former, Ce^{3+} cations in the subsurface layer lie 1.9 Å below those in the surface layer, whereas in the latter, subsurface Ca^{2+} cations lie 3.0 Å below the surface. The removed carbonate anion, which served to neutralize subsurface cations as it extended below either surface, is re-placed with a ligand that does not penetrate below the surface into the vacancy (See Figures S12 and S14 and Tables S8 and S10). As a result, the subsurface cation at the vacancy site remains under-coordinated to some degree. Calcite, with subsurface cations farther from the surface-bound adsorbate, is even more de-stabilized by replacement of CO_3^{2-} with SHA^{2-} than is bastnäsite.
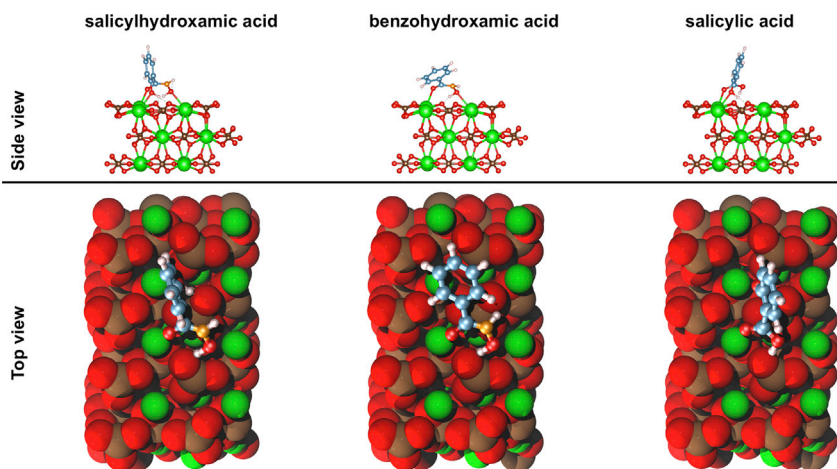
Figure 2. DFT Structures of the Most Stable Adsorption Configurations of Each Ligand on Calcite-[10$\bar{1}$4]

Charge neutrality is maintained by having acidic proton(s) either on a ligand or surface-CO_3^{2-}. For clarity, side views show only the top three layers of calcite slabs. Color scheme: Ca, green; C, brown/cyan; O, red; N, orange; H, white. See also Figure S2 for a detailed depiction of interactions contributing to adsorption.

SA, with a smaller carboxylate functional group (d(O-O) = 2.24 Å) than the hydroxamate group in SHA (d(O-O) = 2.74 Å), is more apt to fit into a carbonate vacancy site, allowing the carboxylate group to reach into the defect to interact with subsurface cations in both bastnäsite and calcite (see Figures S13 and S15 and Tables S9 and S11). Nevertheless, SA and SHA show the same number of interactions with cations at carbonate vacancy sites on the same surface (see Figures S4 and S5), and both molecules show similar replacement energies on bastnäsite prior to correcting for experimental pH (i.e., applying Equation S2 without including E_{corr} values yields 39.3 kJ/mol for SHA and 36.6 kJ/mol for SA). In contrast, the replacement energy of SA on calcite is 23.0 kJ/mol less than that of SHA, before considering pH corrections (i.e., 96.5 kJ/mol for SHA and 73.5 kJ/mol for SA). With a deeper subsurface layer, defective calcite is more effectively stabilized by the penetration of SA into the vacancy site than is defective bastnäsite. As a result, the energy difference between replacement of SA on bastnäsite and on calcite ($\Delta E_{rep, \, SA, \, bastnäsite-calcite}$ = −36.9 kJ/mol) is smaller than for SHA ($\Delta E_{rep, \, SHA, \, bastnäsite-calcite}$ = −57.2 kJ/mol), which does not penetrate into either surface. This translates directly to greater selectivity for bastnäsite over calcite by SHA than by SA, in agreement with the microflotation results above. Furthermore, after accounting for pH corrections, according to Equation S3, we find more facile replacement of CO_3^{2-} by SHA than by SA on both surfaces (see Table S1).

Vibrational Sum Frequency Generation Spectroscopy Experiments

The vSFG spectra probing the C-H stretching region for the three ligands studied at the bastnäsite-[10$\bar{1}$0]-water interface are shown in Figure 3A at surface saturation. In all cases, the signals from the ligand-adsorption species were much weaker compared with measurements on ligands with alkyl tails (Sutton et al., 2020; Wanhala et al., 2019). The weak signal qualitatively suggests that the ligands are arranged such that the transition dipoles are oriented more parallel to the interfacial plane. This is supported by DFT calculations that show that SHA and BHA prefer to orient with the aromatic rings more parallel to the interface, where vSFG signals would vanish due to in-plane rotational isotropy. Bands near 2,850–2,950 cm^{-1} are associated with vibrations in the respective ligands and can be attributed to a redshifted O-H stretch of the carboxylic acid or phenolic groups or aromatic C-H stretches (Doughty et al., 2017; Gotch et al., 1991; Kandziolka et al., 2014). DFT results presented above support the possibility that these peaks are O-H stretches, whereas Raman measurements (*vide infra*) suggest there might be some weakening of the aromatic ring that would lower the C-H stretching frequency. Where present, features near 3,050 cm^{-1} are often attributed to the C-H stretches of aromatic rings; however, the absence of this mode in SA suggests that it could be due to a redshifted N-H stretch arising from hydrogen-bonding interactions, as further supported in the literature (Voss et al., 2018). Future measurements and calculations would aid in a definitive assignment.
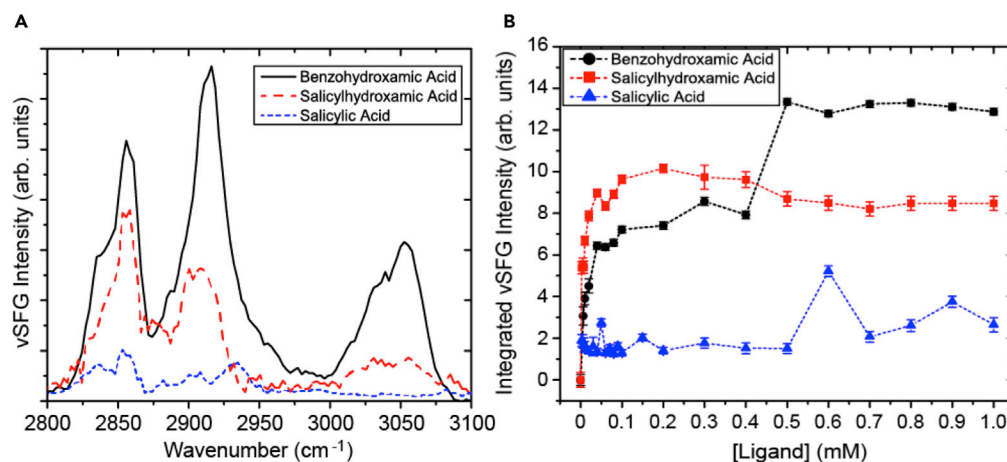
Figure 3. vSFG Results for SA (Blue), SHA (Red), and BHA (Black) Ligands at Bastnäsite-[10$\bar{1}$0]-Aqueous Interfaces

(A) Spectra at surface saturation in the 2,800 to 3,100-cm^{-1} region.

(B) Adsorption isotherms from 0 to 1 mM ligand concentration. Error bars show a standard deviation across three trials. See also Figure S16.

Spectrally integrating the vSFG spectra and plotting the resulting intensity versus bulk ligand concentration generates the isotherms shown in Figure 3B. The binding equilibria captured by these isotherms can be described by

$$ligand + bastnäsite \overset{K_{ads}}{\longleftrightarrow} ligand@bastnäsite$$

such that K_{ads} is the adsorption equilibrium constant. The adsorption isotherms were fit up to a concentration of 0.3 mM using a standard Langmuir isotherm of the form (fits shown in Figure S16):

$$I_{vSFG}(C) = \left[\frac{\alpha \cdot C \cdot K_{ads}}{1 + C \cdot K_{ads}}\right]^2 \qquad \text{(Equation 1)}$$

where α is an amplitude related to the maximum coverage and C is the ligand concentration (Doughty et al., 2016; Wanhala et al., 2019). The extracted equilibrium adsorption constants at 296 K were $K_{ads} = 191 \pm 40 \, mM^{-1}$ for BHA and $K_{ads} = 659 \pm 134 \, mM^{-1}$ for SHA. The corresponding adsorption free energies are then $\Delta G_{ads} = -29.9 \pm 0.5 kJ/mol$ for BHA and $\Delta G_{ads} = -33.0 \pm 0.5 kJ/mol$ for SHA. In agreement with DFT results (Table 2), the adsorption strengths of the two ligands are very similar to one another, indicating that they should perform similarly in flotation, assuming they occupy the same surface area and operate in a monolayer regime. Binding of SA to bastnäsite was observed as a small change in signal and could not be fit to an isotherm model. Notably, at a concentration near 0.5 mM—above the isotherm saturation (i.e., ~0.3 mM)—we see an increase in signal for BHA, whereas a gradual decrease in signal is observed for SHA (Figure 3B). The increase in signal of BHA can be rationalized as a coverage-induced reorientation of the ligands on the surface. Specifically, at lower coverages, the molecules arrange such that the aromatic rings are lying more parallel to the interface, but as the surface becomes crowded they begin standing more upright to accommodate an overall larger number of ligands. This increase in the vSFG signal would then reflect an increase in the maximum number density of ligands and their orientational rearrangement out of the surface plane. Such a case of aromatic rings packing perpendicular to the surface at higher coverages may preclude BHA multilayer formation.

The lack of signal increase for SHA at higher concentrations suggests that SHA assumes a mostly surface-parallel orientation at low and high coverages, consistent with the DFT result showing anchoring by the phenolic group to interfacial binding sites, thereby limiting its ability to reorient at higher coverages. The slight decrease in signal suggests that, in contrast to BHA, SHA multilayers are being formed, decreasing vSFG signals due to increasing local symmetry. SA shows a weak signal throughout, with a subtle increase at higher concentrations, suggesting that, consistent with DFT results, adsorption is much weaker than for the other two ligands, even at elevated SA concentrations.
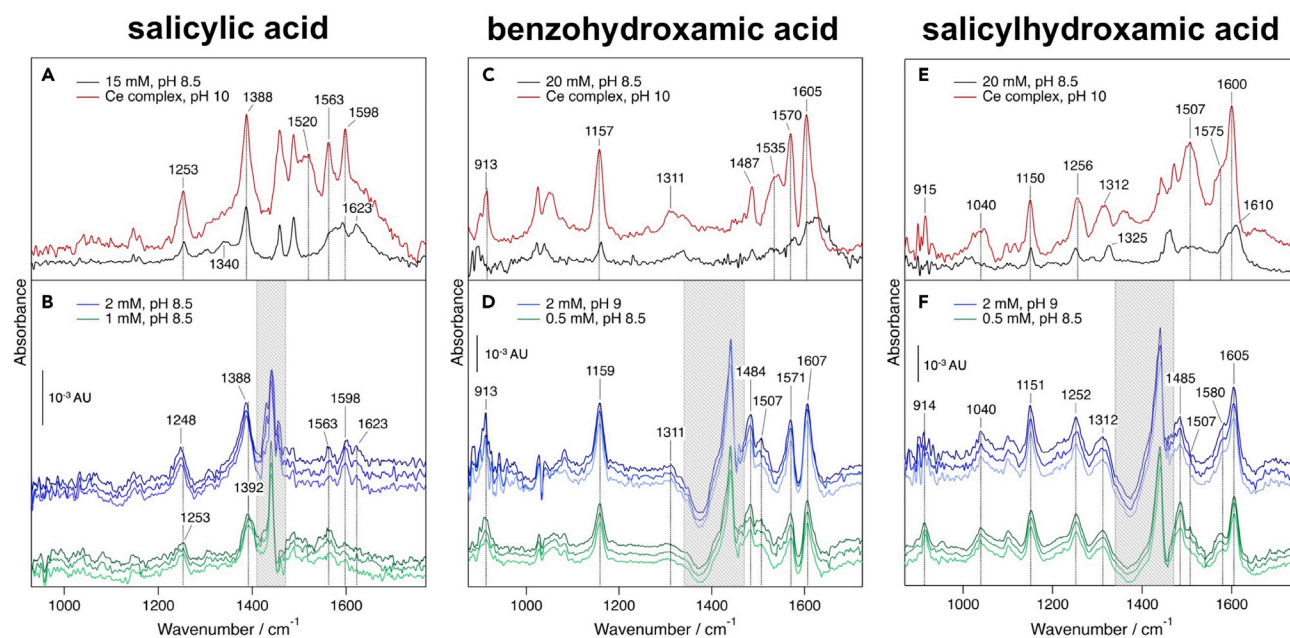
Figure 4. ATR-FTIR Spectra of Pure Ligands (Black), Ligands Complexed with Ce³⁺ (Red), and Spectra of Ligands Adsorbed onto Bastnäsite after 20, 40, and 60 min at Two Different Ligand Concentrations (Green and Blue)

(A) Pure SA and SA-Ce³⁺ complex. (B) SA on bastnäsite.

(C) Pure BHA and BHA-Ce³⁺ complex. (D) BHA on bastnäsite.

(E Pure SHA and SHA-Ce³⁺ complex. (F) SHA on bastnäsite. Curves are vertically offset for clarity. Peaks in shaded regions cannot be resolved owing to imperfect subtraction of the bastnäsite background.

Attenuated Total Reflection-Fourier Transform Infrared Spectroscopy Experiments

Spectra of SA adsorbed to bastnäsite *in situ* at pH 8.5 are shown in Figure 4B. Peaks corresponding to adsorbed SA are very weak, suggesting poor adsorption of SA onto bastnäsite, in agreement with vSFG intensities and DFT energies. At 1 mM concentration (green traces), the symmetric and asymmetric COO^- stretching bands are visible at 1,392 and 1,563 cm^{-1}, respectively. Although the peak at 1,392 cm^{-1} overlaps the intense CO_3 stretching vibration of the underlying bastnäsite solid (shaded region), it can still be clearly differentiated from the subtracted background. Decreased separation of these frequencies relative to those of the free ligand (Figure 4A, black trace) indicates binding of the carboxylate group via either a bidentate chelate or bridging mechanism (Korpany et al., 2017). Phenolic C-O stretching shows a broadened peak at 1,253 cm^{-1}, similar to that in the spectrum of the aqueous SA-Ce³⁺ complex (red trace).

At 2 mM concentration (Figure 4B, blue traces), more SA adsorbs, slightly improving the signal to noise ratio of adsorbed-ligand peaks. However, the peak positions are changed relative to the 1 mM spectra. The COO^- asymmetric stretching peak at 1,563 cm^{-1} is smaller than the neighboring peak at 1,598 cm^{-1}. The symmetric stretching frequency is decreased to 1,388 cm^{-1}, with unresolved intensity on the low-wavenumber side of this peak. These bands are more similar to those of the uncomplexed ligand than to the low-concentration SA-bastnäsite spectra, indicating a weaker physisorption at higher coverages, perhaps in addition to the chemisorbed layer. The phenolic C-O stretch now shows a predominant peak that is redshifted relative to the aqueous Ce³⁺ complex, to 1,248 cm^{-1}, primarily suggesting interaction of the phenolic group with the surface and/or among surface-bound layers of SA, likely through hydrogen bonding (Thomas and Kelley, 2008).

Adsorption of hydroxamate ligands onto mineral surfaces has previously been measured using ATR-FTIR (Borer et al., 2009; Sreenivas and Padmanabhan, 2002; Wanhala et al., 2019). In previous investigations, the adsorption mechanisms of alkyl hydroxamates were clearly reflected in the strong C=O stretching band (Cui et al., 2012). Figure 4D shows time-resolved spectra of BHA adsorbed to bastnäsite. Strong peaks at 1,607 and 1,571 cm^{-1} appear, consistent with the spectrum of the Ce-complexed BHA solution
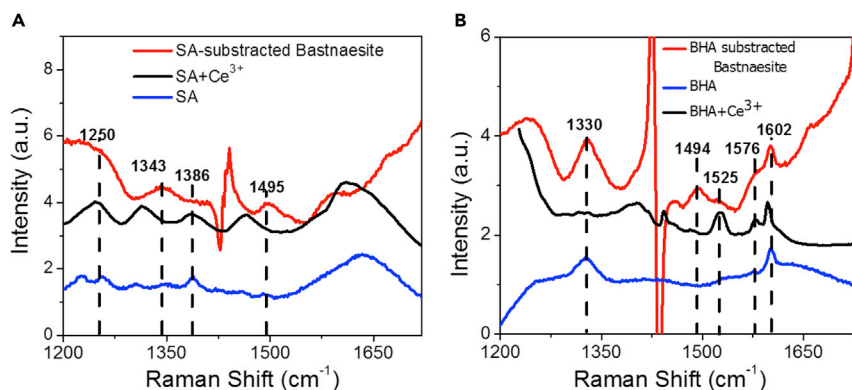
Figure 5. Raman Spectra of Aqueous Ligand Solutions (Blue), Complex of Ligand + Ce^{3+} Prepared in Aqueous Solution, pH 8.5 (Black), and Bastnäsite-[10$\bar{1}$0] with Ligand (Red)

Red bastnäsite + ligand spectra result from the subtraction of the spectrum of the bastnäsite crystal (See Figure S17) prior to ligand exposure.

(A) SA, 17 mM.

(B) BHA, 18 mM.

(Figure 4C, red trace). The sharp peak at 1,159 cm^{-1}, also in agreement with the spectrum of the solution-phase complex, is reported in the literature for BHA as a combination band with contributions from C-N, N-O, and aromatic C-C stretching and C-H bending (Al-Saadi, 2012). Finally, a peak appears at 913 cm^{-1} in the spectra of bastnäsite-adsorbed species, assigned to N-O stretching and CNO deformation of the hydroxamate functional group. Although this peak exhibits poor signal to noise ratio, it appears much more clearly, and at higher frequency, than in the spectrum of aqueous BHA (black trace). Together, these results suggest that BHA adsorbs via bridging or a bidentate chelate, which is expected from Ce-hydroxamic acid complexes in solution (Sarvaramini et al., 2016).

Spectra of SHA adsorbed to bastnäsite are shown in Figure 4F. At 0.5 mM (green traces), clear peaks corresponding to the adsorbed ligand are apparent in the spectra. The sharp peak at 1,605 cm^{-1} resembles that in the spectrum of the aqueous-phase Ce-complexed ligand (Figure 4E, red trace). This well-resolved band involves stretching motions of both the hydroxamate C=O bond and the aromatic ring, suggesting chelated SHA, in agreement with DFT results shown in Figure S3 and FTIR spectra of SHA-bastnäsite systems reported previously (Xiong et al., 2020). A partially resolved band at 1,575 cm^{-1}, assigned to C-N stretching/N-H bending (amide II) of the hydroxamate moiety (Brennan et al., 2016; Zhao et al., 2019), as well as aromatic-ring stretching, is consistent with the spectrum of the aqueous complex; however, this band shows increased separation from the C=O stretching feature when compared with the spectrum of the aqueous-phase Ce-complexed ligand. A redshift from higher frequencies may be due to hydrogen-bond donation by the N-H moiety (Arunan et al., 2011; Pauling, 1931), in line with DFT results (Figure 2) and vSFG spectral features.

At 2 mM concentration, the spectra of adsorbed SHA (Figure 4F, blue traces) are slightly different. For example, the peak at 1,507 cm^{-1}, which appears upon complexation, contributes less to the overall intensity than at low concentration, suggesting that some of the SHA at the surface is uncomplexed, consistent with multilayer formation at elevated concentrations, in agreement with vSFG results. The hydroxamate mode around 1,580 cm^{-1} is less resolved from the carbonyl stretching, with similar separation between both frequencies as in the aqueous SHA-Ce complex. This perhaps suggests that the hydrogen bond donated by the hydroxamate N-H moiety is weaker or absent in physisorbed SHA.

Raman Spectroscopy Experiments

The Raman spectrum for SA at the bastnäsite-[10$\bar{1}$0] surface is shown as the red trace in Figure 5A. The spectrum of bastnäsite prior to SA exposure (Figure S17, green trace) was subtracted from the SA-bastnäsite spectrum and scaled to match the intensity of the pure bastnäsite peak at 1,430 cm^{-1} (Frost et al., 2013).

The spectrum of SA on bastnäsite shows strong features at 1,343 and 1,495 cm^{-1}. The band at 1,495 cm^{-1} is assigned to changes in C-C stretching in the aromatic ring in SA (Green, 1977; Humbert et al., 1998). This band is shifted to higher frequency in comparison with that of the aqueous Ce-complex (Figure 5A, black trace), which suggests a greater distortion of the ring vibration of SA in the presence of bastnäsite. The distortion of the aromatic ring vibrations as a result of the SA interaction with metallic surfaces has been reported in the literature (Alvarez-Ros et al., 2000). The intensity of the ring vibration may be influenced by how molecules are packed on the surface. For instance, a confinement of the ring to the surface may suppress ring vibrations, whereas a vertical SA orientation, with the ring pointing away from the bastnäsite surface, would allow for the stretching of C-C bonds as observed in our case. A vertical orientation of SA on the surface is consistent with DFT structures of SA on bastnäsite (Figure 1 and S3). In the case of SA-bastnäsite, the strong band at 1,343 cm^{-1}, which contains contributions from both the C–O (carboxylic) and C–OH (phenolic) groups, is shifted to a higher frequency relative to the band near 1,313 cm^{-1} in the aqueous SA-Ce^{3+} complex, suggesting the participation of these groups in the interaction with the surface, in agreement with DFT and ATR-FTIR results. In addition, we acknowledge that ring vibrations might also contribute to this spectral feature. Literature reports (Alvarez-Ros et al., 2000; Green, 1977; Humbert et al., 1998) suggest that SA can bind to the surface electrostatically, through the involvement of coordination bonds, and/or through the formation of hydrogen bonds. The Raman spectrum of SA on the surface is notably distinct from that of SA bound to Ce^{3+} in solution, suggesting that either the adsorption mechanism of SA to Ce^{3+} in bastnäsite differs greatly from that in solution or that SA is not specific for Ce^{3+} and can bind to surface or other ions in bastnäsite. The role of other ions in collector adsorption onto bastnäsite has been discussed previously (Cao et al., 2018).

The crystal-subtracted spectrum of BHA on the surface of bastnäsite is presented as the red trace in Figure 5B. Vibrational bands of pure BHA (blue trace) at 1,330 and 1,602 cm^{-1} are shown in the bastnäsite-adsorbed spectrum. Furthermore, a comparison of the subtracted-bastnäsite spectrum with that of the aqueous BHA-Ce^{3+} complex (black trace) reveals features that are common to both spectra at around 1,494, 1,525, and 1,576 cm^{-1}. Together, this suggests similar complexes are formed both on the surface and in aqueous solution. However, the positions of some bands differ from those in the solution-phase spectrum, indicative of different strengths of interaction. Differences in interaction strength between BHA and metal ions in solution and at surfaces are also reported in the literature (Blajiev et al., 2006). The band at 1,494 cm^{-1} (Blajiev et al., 2006) suggests an involvement of the hydroxamate moiety in the interaction with the surface, consistent with ATR-FTIR and DFT results.

The bastnäsite-subtracted SHA-crystal spectrum (Figure S18) does not show well-defined peaks that correlate with those found in the aqueous-phase spectrum with Ce^{3+}. There are, however, some weak peaks that can be associated with the chemical fingerprint of pure SHA in water. The low intensity of the peaks cannot be explained by a fluorescence background, as signal to noise ratios are on average twice as high for SHA as for SA or BHA. Although such a spectrum is suggestive of weak adsorption of SHA on the bastnäsite surface, an alternative explanation could be that SHA lies flat on the surface, as suggested by DFT and vSFG results, thus reducing the Raman signal from the interface.

DISCUSSION

A multifaceted approach enlisting microflotation experiments, DFT calculations, and vSFG, ATR-FTIR, and Raman spectroscopies explored the adsorption of SHA onto the surface of bastnäsite. By comparing the results from complementary theoretical and surface-sensitive spectroscopic methods with analogous ones for BHA and SA, we obtain a mutually consistent, molecular-level understanding of the relationship between the structure of SHA and its adsorption onto bastnäsite and its selectivity for bastnäsite over calcite in froth flotation.

The DFT, vSFG, and ATR-FTIR results show that the hydroxamic acid moiety in SHA/BHA leads to stronger adsorption than the carboxylic acid moiety in SA onto bastnäsite surfaces, although DFT structures and ATR-FTIR spectra show that both moieties present similar binding modes. Furthermore, DFT, vSFG, and Raman results, combined, reveal that the aromatic ring in SHA tends to lie parallel to the bastnäsite-[10$\bar{1}$0] surface at both monolayer and multilayer concentrations, whereas BHA, which differs in structure from SHA only through the omission of the *ortho* phenol group, shows a ring oriented more perpendicular to the surface at high ligand concentrations.

The contrast of orientations of BHA and SHA on bastnäsite and calcite highlights the role of the phenolic moiety in adsorption. Despite the disparate adsorption orientations, however, the phenolic moiety does not affect the adsorption strength of SHA onto an ideal bastnäsite-[10$\bar{1}$0] surface. SHA, as revealed through DFT and vSFG results, has a similar binding energy as BHA, perhaps resulting from the recognition of the surface by the common hydroxamic acid moiety. The similarity in energies, in contrast to dissimilar micro-flotation results, suggests that the collector's performance in bastnäsite flotation experiments may not be captured by considering solely pristine mineral surfaces. DFT results highlight the need to also consider defective surfaces, as are likely present in mined ores. Studies at single-carbonate-vacancy-defect sites reveal that the large hydroxamic acid moiety in SHA is unable to penetrate beyond the surface into the defect, leaving an unstable metal cation at the subsurface. This instability, due to differences in the cationic spacing on each surface, is greater on the most stable calcite surface than on the most stable bastnäsite surface, leading to adsorption differences on these surfaces and thereby contributing to the efficacy of hydroxamic acid collectors in selective froth flotation.

Finally, our unique surface-sensitive approach to SHA recognition of the bastnäsite surface paves the way for a detailed account of nonbonding interactions in beneficiation systems. Although mechanistic studies of flotation have generally focused on the chelation of the hydroxamate moiety with metal ions, our piecewise approach to understanding SHA adsorption reveals the integral role of hydrogen-bonding interactions in flotation, which have only begun to be described. Future work in this field shall continue to employ parallel studies of ligand-bastnäsite and ligand-gangue interactions on both pristine and defective surfaces in order to relate a comparative molecular-level description to flotation efficacy in terms of the recognition of surfaces. Probes of hydrogen bonding must also be extended toward a complete description of interactions among the ligand, the surface, and explicit water molecules on the surface and in immediate solvation shells. We anticipate that our fundamental results relating the structure of SHA to its adsorption onto bastnäsite surfaces and its beneficiation efficacy will provide insight into the selection and design of new ligands as candidates for bastnäsite collectors.

Limitations of the Study

- Microflotation results presented herein reflect a single trial for each system under the conditions presented in the Experimental Procedures section of this work. However, these results are taken from an extensive design of experiments system that included 18 collectors each, tested at a combination of three different collector concentrations and three pH values. The values reported herein reflect the most successful conditions tested in terms of recovery and grade.

- DFT calculations are limited by a realistic description of surface charge and the protonation state of the ligand under experimental conditions. We expect, at a pH of 8.5, SHA and SA to be monoanionic. Owing to prohibitive computational expense, the model used in this work does not provide explicit water molecules, which would serve to stabilize this anion and its conjugate proton. As such, we instead provide two charge-balanced systems, one in which all protons are found near the adsorbed ligand and another in which two protons have been donated. In the latter, the dianionic ligand replaces a CO_3^{2-} dianion on the surface.

- As adsorbate frequencies likely shift as a result of adsorption, the peaks presented in vSFG experiments cannot be definitively assigned without isotopic substitution or costly vibrational spectral calculations, which are beyond the scope of this paper.

- In Raman experiments, all signals coming from the bare crystal cannot be completely removed owing to intrinsic inhomogeneities of the mineral. As such, the intensity of the Raman signals are dependent on the location probed on the crystal surface. Additionally, imperfect background subtraction of bastnäsite background in ATR-FTIR spectra leaves bands that overlap with adsorbate vibrational frequencies.

Resource Availability

Lead Contact

Further information and requests for resources and reagents should be directed to and will be fulfilled by the Lead Contact, Vyacheslav S. Bryantsev (bryantsevv@ornl.gov).

AUTHOR CONTRIBUTIONS

R.C.C. analyzed DFT results, prepared figures, and contributed to writing the paper. A.U.C. conducted vSFG experiments. A.K.W. conducted and analyzed ATR-FTIR experiments, prepared figures, and contributed to writing the paper. V.B. conducted and analyzed Raman experiments, provided figures, and contributed to writing the paper. S.R. contributed to DFT calculations. P.C.K. and D.E. conducted microflotation experiments. S.J.-P. identified hydroxamic acids for use in this project and distributed chemicals used in this work to team members. A.K. performed and analyzed Raman experiments. R.L.S. performed surface characterization and spectral analysis. A.G.S. and C.G.A. oversaw experiments and provided insights toward the manuscript. B.D. conducted and analyzed vSFG experiments and contributed to writing the paper. V.S.B. performed and analyzed DFT calculations and oversaw the collaboration leading to this manuscript.

DECLARATION OF INTERESTS

The authors declare no competing interests.

REFERENCES

Al-Saadi, A.A. (2012). Conformational analysis and vibrational assignments of benzohydroxamic acid and benzohydrazide. J. Mol. Struct. *1023*, 115–122.

Alvarez-Ros, M.C., Sánchez-Cortés, S., and García-Ramos, J.V. (2000). Vibrational study of the

salicylate interaction with metallic ions and surfaces. Spectrochim. Acta A: Mol. Biomol. Spectrosc. *56*, 2471–2477.

Anderson, C.D. (2015). Improved Understanding of Rare Earth Surface Chemistry and its

Application to Froth Flotation (Colorado School of Mines. Arthur Lakes Library).

Arunan, E., Desiraju Gautam, R., Klein Roger, A., Sadlej, J., Scheiner, S., Alkorta, I., Clary David, C., Crabtree Robert, H., Dannenberg Joseph, J., Hobza, P., et al. (2011). Defining the hydrogen

bond: an account (IUPAC Technical Report). Pure Appl. Chem. 1619.

Assis, S.M., Montenegro, L.C.M., and Peres, A.E.C. (1996). Utilisation of hydroxamates in minerals froth flotation. Miner Eng. 9, 103–114.

Blajiev, O., Terryn, H., Hubin, A., Soukupova, L., and Geerlings, P. (2006). Adsorption of some benzohydroxamic acid derivatives on copper oxide: assignment and interpretation of SERS spectra. J. Raman Spectrosc. 37, 777–788.

Borer, P., Hug, S.J., Sulzberger, B., Kraemer, S.M., and Kretzschmar, R. (2009). ATR-FTIR spectroscopic study of the adsorption of desferrioxamine B and aerobactin to the surface of lepidocrocite (γ-FeOOH). Geochim. Cosmochim. Acta 73, 4661–4672.

Brennan, B.J., Chen, J., Rudshteyn, B., Chaudhuri, S., Mercado, B.Q., Batista, V.S., Crabtree, R.H., and Brudvig, G.W. (2016). Molecular titanium–hydroxamate complexes as models for TiO_2 surface binding. Chem. Commun. 52, 2972–2975.

Cao, S., Cao, Y., Liao, Y., and Ma, Z. (2018). Depression mechanism of strontium ions in bastnaesite flotation with salicylhydroxamic acid as collector. Minerals 8, 66.

Cao, Z., Cao, Y., Qu, Q., Zhang, J., and Mu, Y. (2019). Separation of bastnäsite from fluorite using ethylenediamine tetraacetic acid as depressant. Miner Eng. 134, 134–141.

Cases, J., and Villieras, F. (1992). The mechanisms of collector adsorption-abstraction (ionic and non-ionic surfactants) on heterogeneous surfaces. In Innovations in Flotation Technology (Springer), pp. 25–55.

Castor, S.B. (2008). The Mountain Pass rare-earth carbonatite and associated ultrapotassic rocks, California. Can. Mineral. 46, 779–806.

Cui, H., and Anderson, C.G. (2017a). Alternative flowsheet for rare earth beneficiation of Bear Lodge ore. Miner Eng. 110, 166–178.

Cui, H., and Anderson, C.G. (2017b). Fundamental studies on the surface chemistry of ancylite, calcite, and strontianite. J. Sustain. Metall. 3, 48–61.

Cui, J., Hope, G.A., and Buckley, A.N. (2012). Spectroscopic investigation of the interaction of hydroxamate with bastnaesite (cerium) and rare earth oxides. Miner Eng. 36-38, 91–99.

Doughty, B., Srinivasan, S.G., Bryantsev, V.S., Lee, D., Lee, H.N., Ma, Y.-Z., and Lutterman, D.A. (2017). Absolute molecular orientation of isopropanol at ceria (100) surfaces: insight into catalytic selectivity from the interfacial structure. J. Phys. Chem. C 121, 14137–14146.

Doughty, B., Yin, P., and Ma, Y.-Z. (2016). Adsorption, ordering, and local environments of surfactant-encapsulated polyoxometalate ions probed at the air–water interface. Langmuir 32, 8116–8122.

Drew, L.J., Qingrun, M., and Weijun, S. (1990). The Bayan Obo iron-rare-earth-niobium deposits, Inner Mongolia, China. Lithos 26, 43–65.

Eggert, R., Wadia, C., Anderson, C., Bauer, D., Fields, F., Meinert, L., and Taylor, P. (2016). Rare earths: market disruption, innovation, and global supply chains. Annu. Rev. Environ. Resour. 41, 199–222.

Elam, W.A. (2014). Molecular modeling for the design of novel performance chemicals and materials. Yale J. Biol. Med. 87, 604–605.

Espiritu, E.R.L., da Silva, G.R., Azizi, D., Larachi, F., and Waters, K.E. (2018). The effect of dissolved mineral species on bastnäsite, monazite and dolomite flotation using benzohydroxamate collector. Colloids Surf. A Physicochem. Eng. Aspects 539, 319–334.

Everly, D. (2017). Surface Chemistry of Novel Collectors and Their Application to Froth Flotation of Rare Earth Minerals., MSc Thesis (Colorado School of Mines).

Frey, M., Harris, S.G., Holmes, J.M., Nation, D.A., Parsons, S., Tasker, P.A., and Winpenny, R.E.P. (2000). Elucidating the mode of action of a corrosion inhibitor for iron. Chem. A Eur. J. 6, 1407–1415.

Frost, R.L., López, A., Scholz, R., Xi, Y., and Belotti, F.M. (2013). Infrared and Raman spectroscopic characterization of the carbonate mineral huanghoite – and in comparison with selected rare earth carbonates. J. Mol. Struct. 1051, 221–225.

Fuerstenau, M.C., and Peterson, H.D. (1969). Flotation Method for the Recovery of Minerals (Colorado School of Mines Foundation, Inc.).

Gallios, G., and Matis, K. (1992). Flotation of salt-type minerals. In Innovations in Flotation Technology, P. Mavros and K.A. Matis, eds. (Springer), pp. 357–382.

Ganguli, R., and Cook, D.R. (2018). Rare earths: a review of the landscape. MRS Energy Sustain. 5, E9.

Gotch, A.J., Garrett, A.W., and Zwier, T.S. (1991). The Ham bands revisited: spectroscopy and photophysics of the benzene-carbon tetrachloride complex. J. Phys. Chem. 95, 9699–9707.

Green, J.H.S. (1977). Vibrational spectra of benzene derivatives—XX Substituted benzoate ions and benzoic acids. Spectrochim. Acta A Mol. Spectrosc. 33, 575–581.

Humbert, B., Alnot, M., and Quilès, F. (1998). Infrared and Raman spectroscopical studies of salicylic and salicylate derivatives in aqueous solution. Spectrochim. Acta A Mol. Biomol. Spectrosc. 54, 465–476.

Jordens, A., Cheng, Y.P., and Waters, K.E. (2013). A review of the beneficiation of rare earth element bearing minerals. Miner Eng. 41, 97–114.

Jordens, A., Marion, C., Grammatikopoulos, T., Hart, B., and Waters, K.E. (2016). Beneficiation of the Nechalacho rare earth deposit: flotation response using benzohydroxamic acid. Miner Eng. 99, 158–169.

Jordens, A., Marion, C., Kuzmina, O., and Waters, K.E. (2014). Surface chemistry considerations in the flotation of bastnäsite. Miner Eng. 66-68, 119–129.

Kandziolka, M.V., Kidder, M.K., Gill, L., Wu, Z., and Savara, A. (2014). Aromatic–hydroxyl interaction of an alpha-aryl ether lignin model-compound on SBA-15, present at pyrolysis temperatures. Phys. Chem. Chem. Phys. 16, 24188–24193.

Khalil, M.M., El-Deeb, M.M., and Mahmoud, R.K. (2007). Equilibrium studies of binary systems involving lanthanide and actinide metal ions and some selected aliphatic and aromatic monohydroxamic acids. J. Chem. Eng. Data 52, 1571–1579.

Korpany, K.V., Majewski, D.D., Chiu, C.T., Cross, S.N., and Blum, A.S. (2017). Iron oxide surface chemistry: effect of chemical structure on binding in benzoic acid and catechol derivatives. Langmuir 33, 3000–3013.

Krishnamurthy, N., and Gupta, C.K. (2016). Extractive Metallurgy of Rare Earths (CRC Press).

Kynicky, J., Smith, M.P., and Xu, C. (2012). Diversity of rare earth deposits: the key example of China. Elements 8, 361–367.

Li, M., Gao, K., Zhang, D., Duan, H., Ma, L., and Huang, L. (2018). The influence of temperature on rare earth flotation with naphthyl hydroxamic acid. J. Rare Earths 36, 99–107.

Liu, W., Wang, X., and Miller, J.D. (2019). Collector chemistry for bastnaesite flotation – recent developments. Miner. Process. Extr. Metall. Rev. 40, 370–379.

Long, K.R., Van Gosen, B.S., Foley, N.K., and Cordier, D. (2010). The principal rare earth elements deposits of the United States—a summary of domestic deposits and a global perspective. In US Geological Survey Scientific Investigations Report, p. 96.

Mariano, A.N., and Mariano, A., Jr. (2012). Rare earth mining and exploration in North America. Elements 8, 369–376.

Marion, C., Li, R., and Waters, K.E. (2020). A review of reagents applied to rare-earth mineral flotation. Adv. Colloid Interf. Sci. 279, 102142.

Nagaraj, D. (2018). The chemistry and application of chelating or complexing agents in minerals separations. Reagents Mineral. Technol. 257–334.

Nagaraj, D.R. (1992). Process for Improved Precious Metals Recovery from Ores with the Use of Alkylhydroxamate Collectors (American Cyanamid Company).

Nagaraj, D.R., and Farinato, R.S. (2016). Evolution of flotation chemistry and chemicals: a century of innovations and the lingering challenges. Miner Eng. 96-97, 2–14.

Pauling, L. (1931). The nature of the chemical bond. Application of results obtained from the quantum mechanics and from a theory of paramagnetic susceptibility to the structure of molecules. J. Am. Chem. Soc. 53, 1367–1400.

Pradip. (1992). Design of crystal structure-specific surfactants based on molecular recognition at mineral surfaces. Curr. Sci. 63, 180–186.

Pradip, and Fuerstenau, D.W. (1983). The adsorption of hydroxamate on semi-soluble

minerals. Part I: adsorption on barite, Calcite and Bastnaesite. Colloids Surf. 8, 103–119.

Pradip, and Fuerstenau, D.W. (1985). Adsorption of hydroxamate collectors on semisoluble minerals Part II: effect of temperature on adsorption. Colloids Surf. 15, 137–146.

Pradip, and Fuerstenau, D.W. (2013). Design and development of novel flotation reagents for the beneficiation of Mountain Pass rare-earth ore. Mining Metall. Explor. 30, 1–9.

Pradip, and Rai, B. (2003). Molecular modeling and rational design of flotation reagents. Int. J. Miner Process. 72, 95–110.

Pradip, Rai, B., Rao, T.K., Krishnamurthy, S., Vetrivel, R., Mielczarski, J., and Cases, J.M. (2002). Molecular modeling of interactions of diphosphonic acid based surfactants with calcium minerals. Langmuir 18, 932–940.

Ren, J., Lu, S., Song, S., and Niu, J. (1997). A new collector for rare earth mineral flotation. Miner Eng. 10, 1395–1404.

Rio-Echevarria, I.M., White, F.J., Brechin, E.K., Tasker, P.A., and Harris, S.G. (2008). Surface binding vs. sequestration; the uptake of benzohydroxamic acid at iron(III) oxide surfaces. Chem. Commun. 4570–4572.

Sarvaramini, A., Azizi, D., and Larachi, F. (2016). Hydroxamic acid interactions with solvated cerium hydroxides in the flotation of monazite and bastnäsite—experiments and DFT study. Appl. Surf. Sci. 387, 986–995.

Sreenivas, T., and Padmanabhan, N.P.H. (2002). Surface chemistry and flotation of cassiterite with alkyl hydroxamates. Colloids Surf. A Physicochem. Eng. Aspects 205, 47–59.

Srinivasan, S.G., Shivaramaiah, R., Kent, P.R.C., Stack, A.G., Navrotsky, A., Riman, R., Anderko, A., and Bryantsev, V.S. (2016). Crystal structures, surface stability, and water adsorption energies of la-bastnäsite via density functional theory and experimental studies. J. Phys. Chem. C 120, 16767–16781.

Srinivasan, S.G., Shivaramaiah, R., Kent, P.R.C., Stack, A.G., Riman, R., Anderko, A., Navrotsky, A., and Bryantsev, V.S. (2017). A comparative study of surface energies and water adsorption on Ce-bastnäsite, La-bastnäsite, and calcite via density functional theory and water adsorption calorimetry. Phys. Chem. Chem. Phys. 19, 7820–7832.

Sutton, J.E., Roy, S., Chowdhury, A.U., Wu, L., Wanhala, A.K., De Silva, N., Jansone-Popova, S., Hay, B.P., Cheshire, M.C., Windus, T.L., et al. (2020). Molecular recognition at mineral interfaces: implications for the beneficiation of rare earth ores. ACS Appl. Mater. Inter. 14, 16327–16341.

Talens Peiró, L., and Villalba Méndez, G. (2013). Material and energy requirement for rare earth production. JOM 65, 1327–1340.

Thomas, J.E., and Kelley, M.J. (2008). Interaction of mineral surfaces with simple organic molecules by diffuse reflectance IR spectroscopy (DRIFT). J. Colloid Interf. Sci. 322, 516–526.

Tunsu, C., Petranikova, M., Gergorić, M., Ekberg, C., and Retegan, T. (2015). Reclaiming rare earth elements from end-of-life products: a review of the perspectives for urban mining using hydrometallurgical unit operations. Hydrometallurgy 156, 239–258.

Voss, J.M., Fischer, K.C., and Garand, E. (2018). Revealing the structure of isolated peptides: IR-IR predissociation spectroscopy of protonated triglycine isomers. J. Mol. Spectrosc. 347, 28–34.

Wanhala, A.K., Doughty, B., Bryantsev, V.S., Wu, L., Mahurin, S.M., Jansone-Popova, S., Cheshire, M.C., Navrotsky, A., and Stack, A.G. (2019). Adsorption mechanism of alkyl hydroxamic acid onto bastnäsite: fundamental steps toward rational collector design for rare earth elements. J. Colloid Interf. Sci. 553, 210–219.

Waterson, C.N., Tasker, P.A., Farinato, R., Nagaraj, D.R., Shackleton, N., and Morrison, C.A. (2016). A computational and experimental study on the binding of dithio ligands to sperrylite, pentlandite, and platinum. J. Phys. Chem. C 120, 22476–22488.

Xia, L., Hart, B., Chelgani, S., and Douglas, K.. (2014). Hydroxamate collectors for rare earth minerals flotation. Paper presented at: Conference of Metallurgists Proceedings.

Weng, Z., Jowitt, S.M., Mudd, G.M., and Haque, N. (2015). A detailed assessment of global rare earth element resources: opportunities and challenges. Econ. Geol. 110, 1925–1952.

Xiong, W., Deng, J., Zhao, K., Wang, W., Wang, Y., and Wei, D. (2020). Bastnaesite, barite, and calcite flotation behaviors with salicylhydroxamic acid as the collector. Minerals 10, 282.

Yang, K.-F., Fan, H.-R., Santosh, M., Hu, F.-F., and Wang, K.-Y. (2011). Mesoproterozoic carbonatitic magmatism in the Bayan Obo deposit, Inner Mongolia, North China: constraints for the mechanism of super accumulation of rare earth elements. Ore Geol. Rev. 40, 122–131.

Yang, Z., Wu, W., and Bian, X. (2017). Synthesis of 3-hydroxy-2-naphthyl hydroxamic acid collector: flotation performance and adsorption mechanism on bastnaesite. J. South. Afr. Inst. Mining Metall. 117, 593–598.

Yoon, R.-h., and Hilderbrand, T.M. (1986). Purification of Kaolin Clay by Froth Flotation Using Hydroxamate Collectors (Thiele Kaolin Company).

Yu, X., Zhang, R., Yang, S., Liu, C., He, G., Wang, H., and Wang, J. (2020). A novel decanedioic hydroxamic acid collector for the flotation separation of bastnäsite from calcite. Miner Eng. 151, 106306.

Zhang, X., Du, H., Wang, X., and Miller, J.D. (2014). Surface chemistry aspects of bastnaesite flotation with octyl hydroxamate. Int. J. Miner. Process. 133, 29–38.

Zhao, C., Sun, C., Yin, W., and Luo, B. (2019). An investigation of the mechanism of using iron chelate as a collector during scheelite flotation. Miner. Eng. 131, 146–153.

Supplemental Information

A Molecular-Scale Approach

to Rare-Earth Beneficiation: Thinking

Small to Avoid Large Losses

Robert C. Chapleski Jr., Azhad U. Chowdhury, Anna K. Wanhala, Vera Bocharova, Santanu Roy, Philip C. Keller, Dylan Everly, Santa Jansone-Popova, Alexander Kisliuk, Robert L. Sacci, Andrew G. Stack, Corby G. Anderson, Benjamin Doughty, and Vyacheslav S. Bryantsev

Density Functional Theory Data

salicylhydroxamic acid   **benzohydroxamic acid**   **salicylic acid**
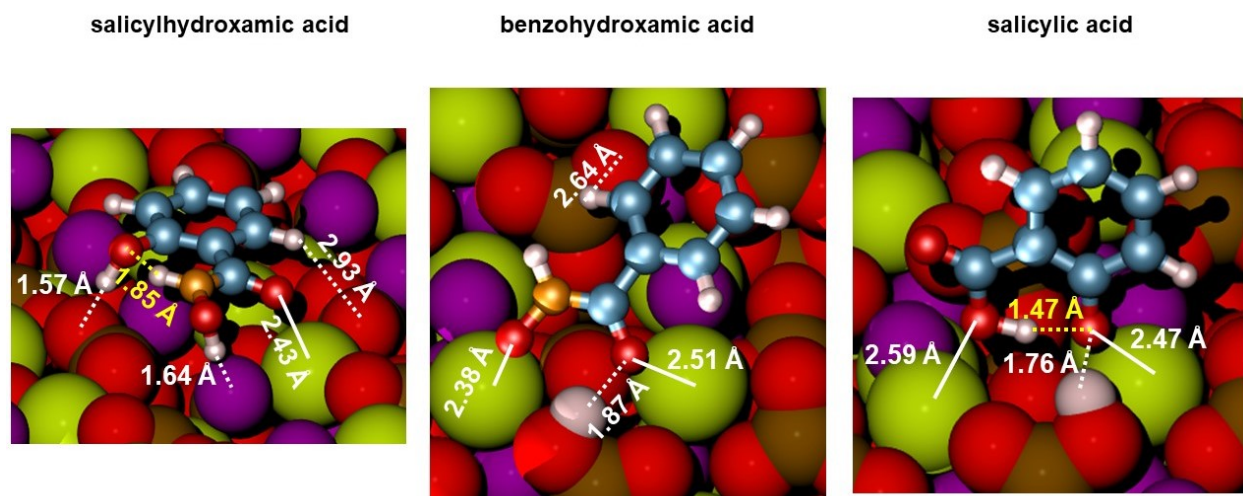

Figure S1. Related to Figure 1: Close-up views of lowest-energy configurations of SHA, BHA, and SA on Ce-bastnäsite-[10$\bar{1}$0] with acidic protons proximal to the adsorbed ligand, as shown in Figure 1 of the main text. Selected interactions are highlighted and presented with corresponding interatomic distances. $Cs_{surface}$-O_{ligand} interactions key to adsorption are identified with solid white lines, surface-ligand hydrogen bonds with dashed white lines, and intra-ligand hydrogen bonds with dashed yellow lines. For atoms, same color scheme as in Figure 1 of the main body of text.

salicylhydroxamic acid   **benzohydroxamic acid**   **salicylic acid**
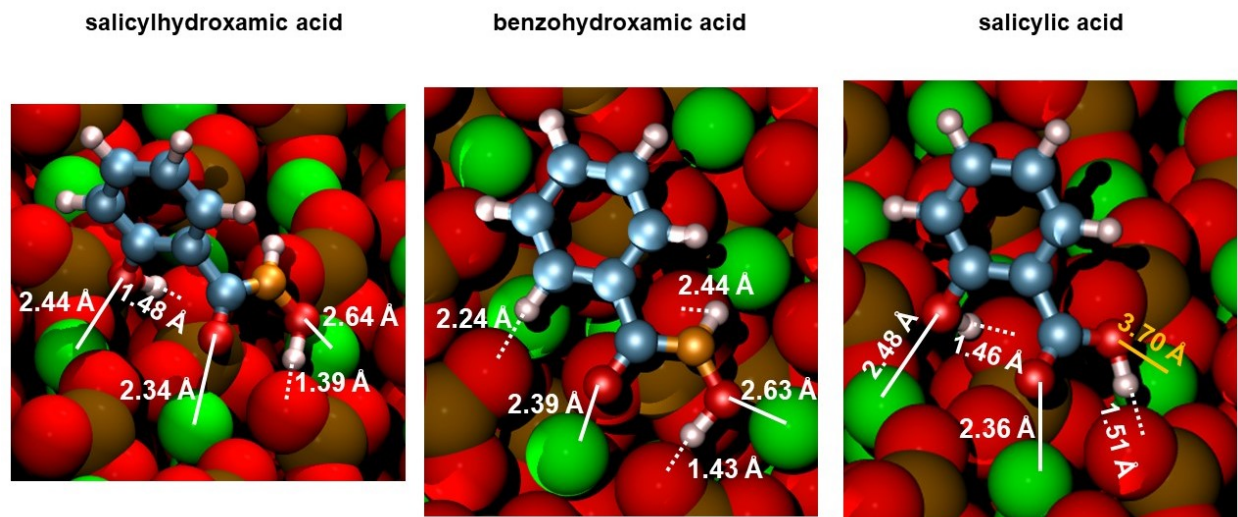
Figure S2. Related to Figure 2: Close-up views of lowest-energy configurations of SHA, BHA, and SA on calcite-[10$\bar{1}$4] with acidic protons proximal to the adsorbed ligand, as shown in Figure 2 of the main text. Selected interactions are highlighted and presented with corresponding interatomic distances. $Ca_{surface}$-O_{ligand} interactions key to adsorption are identified with solid white lines, and surface-ligand hydrogen bonds with dashed white lines. For the sake of comparison to a much shorter analogous $Ca_{surface}$-O_{SHA} interaction (2.64 Å), a longer $Ca_{surface}$-O_{SA} interatomic distance (3.70 Å) is shown in gold. For atoms, same color scheme as in Figure 2 of the main body of text.
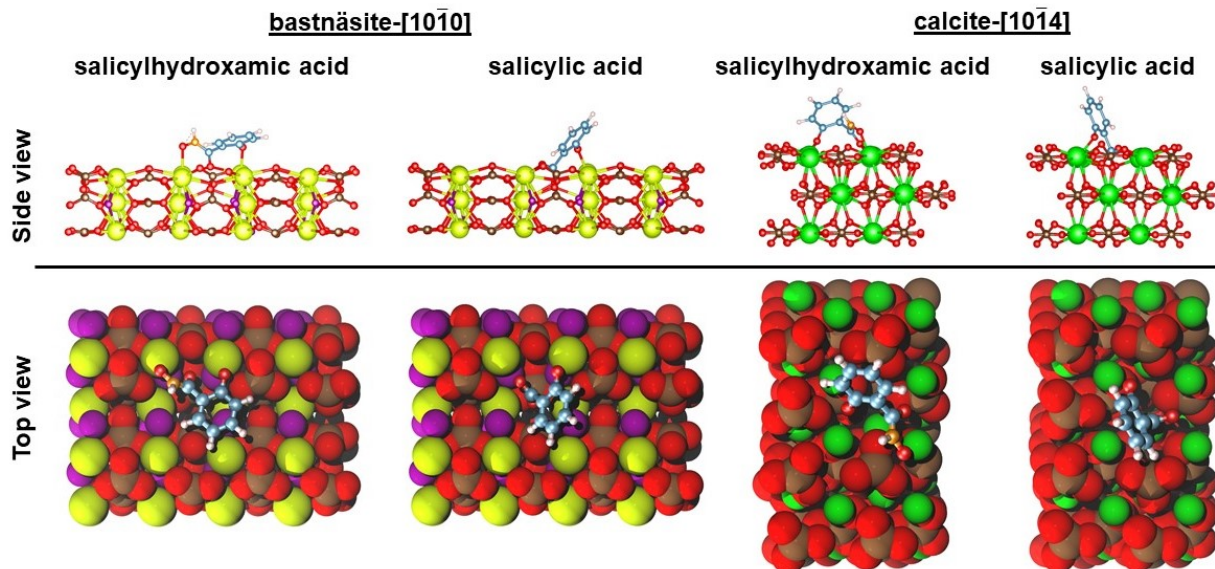
Figure S3. Related to Figures 1 and 2: The most-stable adsorption configurations of SHA and SA on bastnäsite-[10$\overline{1}$0] and calcite-[10$\overline{1}$4], identified from a conformational search using DFT. Charge neutrality is maintained by replacing a surface CO_3^{2-} dianion with a doubly deprotonated collector. For clarity, side views show only the top three layers of mineral slabs. Color schemes are the same as in Figures 1 and 2 of the main text. Detail in Figs. S4 and S5.

Table S1. Related to Scheme 1: Reaction energies (kJ/mol) for the replacement of a surface carbonate dianion on bastnäsite-[10$\overline{1}$0] and calcite-[10$\overline{1}$4] surfaces with a doubly deprotonated collector at pH = 8.5,[a] with dipole and solvent corrections included.

Mineral	Salicylhydroxamic acid (SHA)	Salicylic acid (SA)
bastnäsite-[10$\overline{1}$0]	17.6	41.2
calcite-[10$\overline{1}$4]	74.8	78.0

[a]At pH=8.5, the dominant species are in the singly deprotonated form. Since DFT calculations are performed for neutral, protonated reagent-ligand and carbonic acid species, their energies were corrected by the difference between pH = 8.5 and their pK_{a1} values (Scheme 1 of the main text). See the Transparent Methods section (Eq. S3) for details.
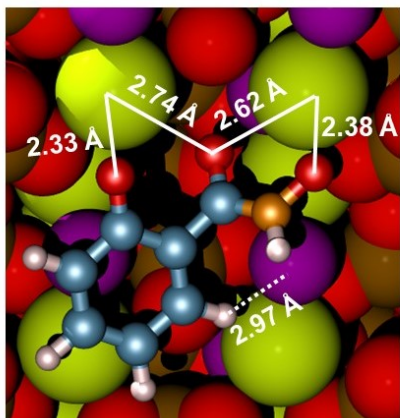
salicylhydroxamic acid   salicylic acid

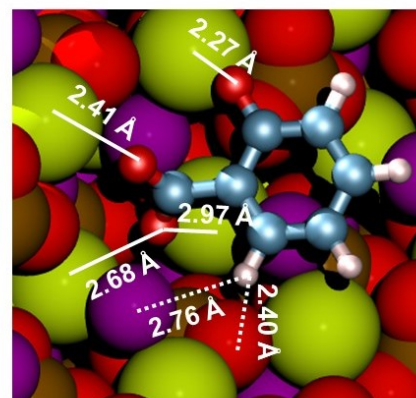**Figure S4. Related to Figure 1**: Close-up views of lowest-energy configurations of SHA and SA on Ce-bastnäsite-[10$\bar{1}$0] following the replacement of a surface CO_3^{2-}, as shown in Figure S3. Selected interactions are highlighted and presented with corresponding interatomic distances. $Cs_{surface}$-O_{ligand} interactions key to adsorption are identified with solid white lines, and surface-ligand hydrogen bonds with dashed white lines. For the SA-bastnäsite system, Ce atoms indicated for the 2.97-Å and 2.68-Å interactions are in the subsurface layer. For atoms, same color scheme as in Figure 1 of the main body of text.
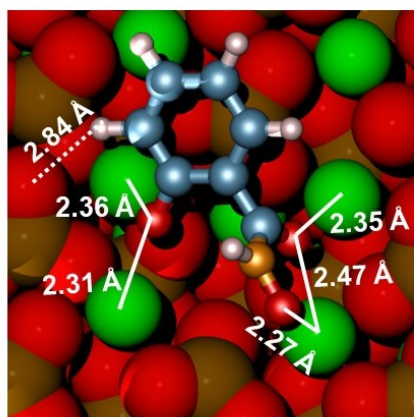
salicylhydroxamic acid   salicylic acid
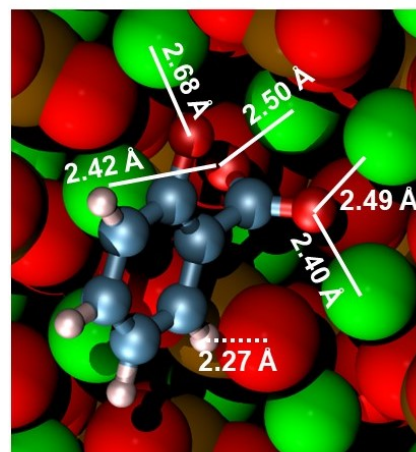
Figure S5. Related to Figure 2: Close-up views of lowest-energy configurations of SHA and SA on calcite-[10$\bar{1}$4] following the replacement of a surface CO_3^{2-}, as shown in Figure S3. Selected interactions are highlighted and presented with corresponding interatomic distances. $Ca_{surface}$-O_{ligand} interactions key to adsorption are identified with solid white lines, and surface-ligand hydrogen bonds with dashed white lines. For the SA-calcite system, Ca atom indicated for the 2.50-Å interaction is in the subsurface layer. For atoms, same color scheme as in Figure 2 of the main body of text.

Figures S6, S7, and S8 show all unique structures optimized in the conformational searches, respectively, for SHA, BHA, and SA adsorption onto bastnäsite-[10$\bar{1}$0], with acidic hydrogens included proximal to the ligand adsorbate. Tables S2, S3, and S4 provide corresponding VASPsol- and dipole-corrected DFT

energies of adsorption for each ligand on bastnäsite-[10$\bar{1}$0], given both according to Eq. (S1) and also relative to the lowest energy configuration, species A. Finally, the vertical displacement (taken along the direction normal to the surface) between the atom in the ligand that is nearest the surface and the highest surface-Ce ion is given as $z_{Ce\text{-}SHA/BHA/SA}$, and the height difference between the lowest ligand atom and the highest of all surface atoms is given as $z_{surface\text{-}SHA/BHA/SA}$.
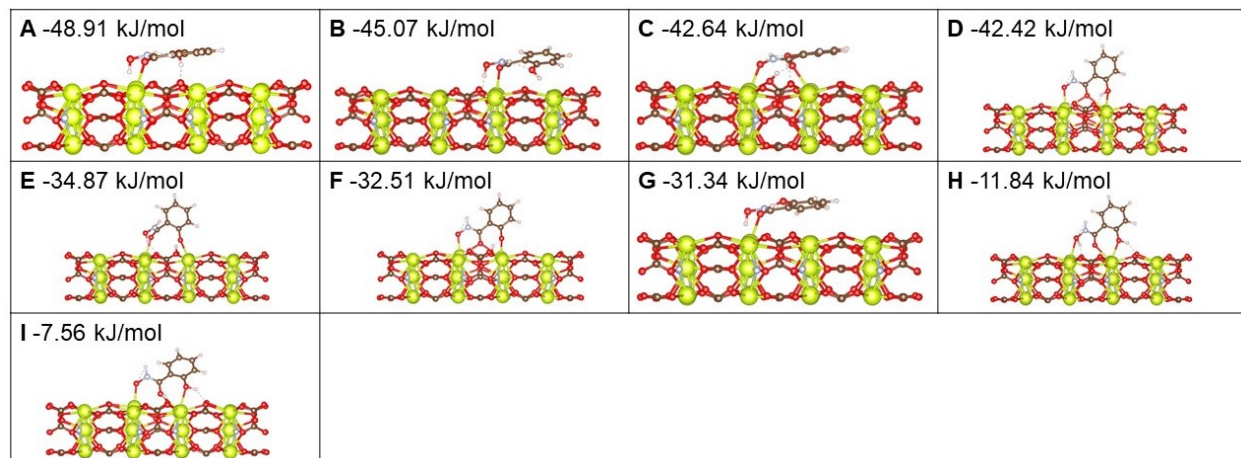
Figure S6. Related to Figure 1 and Table 2: Side views of DFT structures for adsorption of SHA on bastnäsite-[10$\bar{1}$0], including acidic hydrogens. For simplicity, only three layers of the surface slab are shown. Color scheme: Ce: green, C: brown, O: red, F/N: light blue, H: white. Adsorption energies are also given for each structure. Structures result from conformational search described in Transparent Methods section of this file. Species A is that shown in the left panel of Figure 1 of the main text.

Table S2. Related to Table 2: Energies and interatomic coordinates for SHA adsorbed onto bastnäsite-[10$\bar{1}$0]. Structures result from conformational search described in Transparent Methods section of this file. Species A is that shown in the left panel of Figure 1 of the main text.

| Species	Adsorption Energy / kJ mol^{-1}	Energy Relative to Species A / kJ mol^{-1}	$z_{Ce\text{-}SHA}$ / Å	$z_{surf\text{-}SHA}$ / Å
A	-48.91	0.00	1.42	0.89
B	-45.07	3.84	1.47	0.95
C	-42.64	6.28	2.06	0.59
D	-42.42	6.49	1.46	0.86
E	-34.87	14.05	1.86	0.50
F	-32.51	16.41	1.35	0.24
G	-31.34	17.57	1.51	0.89
H	-11.84	37.07	1.75	0.99
I	-7.56	41.35	1.35	0.19

Figure S7. Related to Figure 1 and Table 2: Side views of DFT structures for adsorption of BHA on bastnäsite-[10$\bar{1}$0], including acidic hydrogens. For simplicity, only three layers of the surface slab are shown. Color scheme: Ce: green, C: brown, O: red, F/N: light blue, H: white. Adsorption energies are also given for each structure. Structures result from conformational search described in Transparent Methods section of this file. Species A is that shown in the center panel of Figure 1 of the main text.

Table S3. Related to Figure 1 and Table 2: Energies and interatomic coordinates for BHA adsorbed onto bastnäsite-[10$\bar{1}$0]. Structures result from conformational search described in Transparent Methods section of this file. Species A is that shown in the center panel of Figure 1 of the main text.

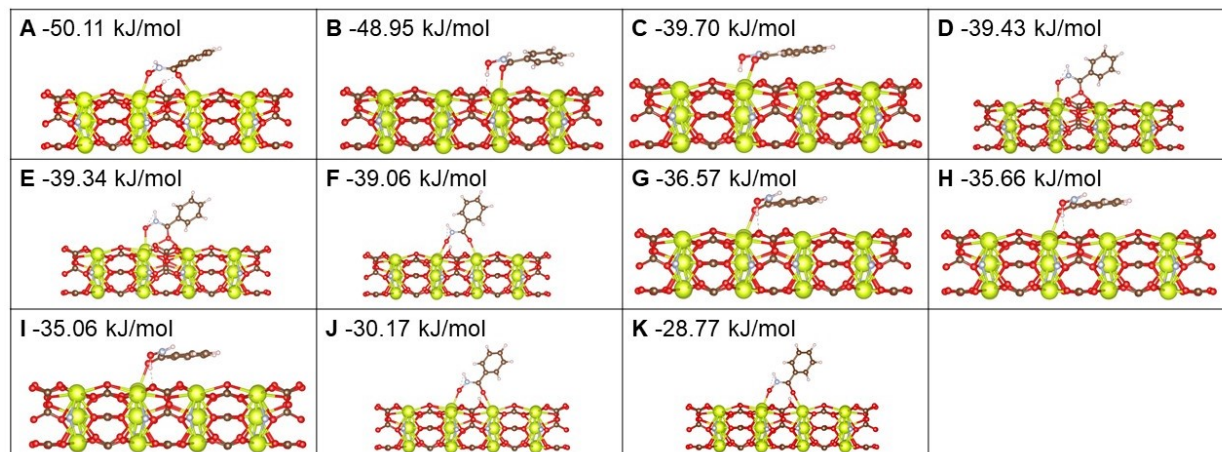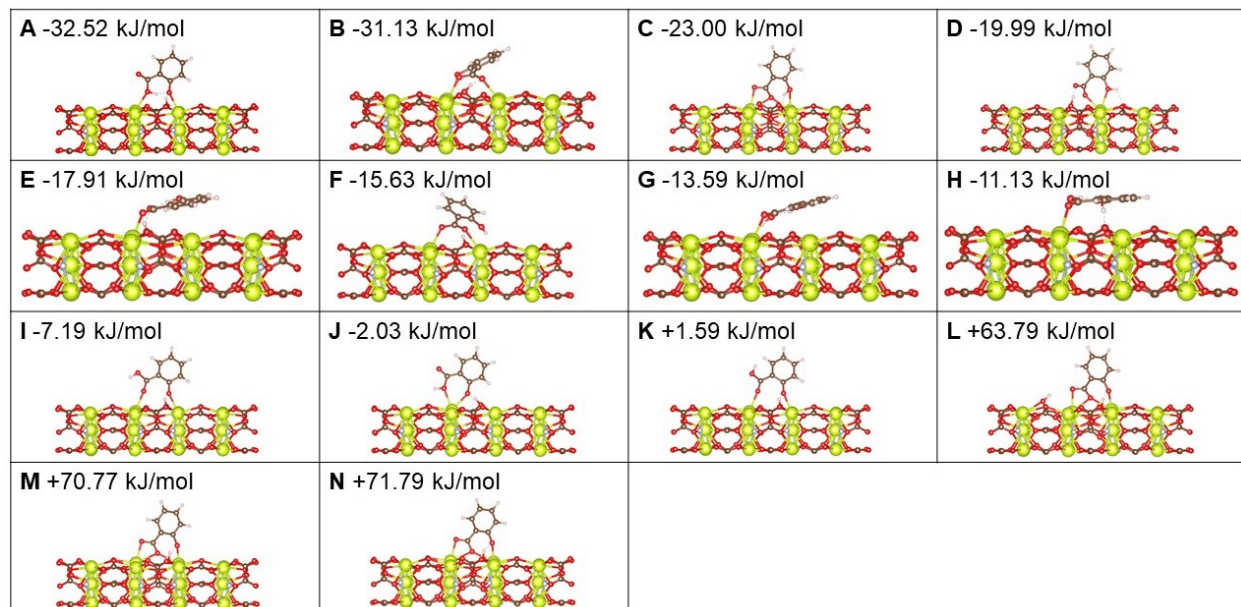| Species	Adsorption Energy / kJ mol^{-1}	Energy Relative to Species A / kJ mol^{-1}	z_{Ce-BHA} / Å	$z_{surf-BHA}$ / Å
A	-50.11	0.00	2.05	0.56
B	-48.95	1.16	1.86	1.28
C	-39.70	10.41	1.43	0.86
D	-39.43	10.68	1.30	0.77
E	-39.34	10.77	1.29	0.76
F	-39.06	11.04	2.07	0.67
G	-36.57	13.54	1.95	1.39
H	-35.66	14.44	1.95	1.38
I	-35.06	15.04	1.93	1.35
J	-30.17	19.94	1.91	0.68
K	-28.77	21.34	1.90	0.69

Figure S8. Related to Figure 1 and Table 2: Side views of DFT structures for adsorption of SA on bastnäsite-[10$\bar{1}$0], including acidic hydrogens. For simplicity, only three layers of the surface slab are shown. Color scheme: Ce: green, C: brown, O: red, F/N: light blue, H: white. Adsorption energies are also given for each structure. Structures result from conformational search described in Transparent Methods section of this file. Species A is that shown in the right panel of Figure 1 of the main text.

Table S4. Related to Figure 1 and Table 2: Energies and interatomic coordinates for SA adsorbed onto bastnäsite-[10$\bar{1}$0]. Structures result from conformational search described in Transparent Methods section of this file. Species A is that shown in the right panel of Figure 1 of the main text.

Species	Adsorption Energy / kJ mol^{-1}	Energy Relative to Species A / kJ mol^{-1}	z_{Ce-SA} / Å	$z_{surf-SA}$ / Å
A	-32.52	0.00	1.89	0.51
B	-31.13	1.39	1.83	0.42
C	-23.00	9.52	1.36	0.70
D	-19.99	12.54	1.77	0.17
E	-17.91	14.62	2.07	0.86
F	-15.63	16.89	1.61	0.36
G	-13.59	18.93	1.40	0.81
H	-11.13	21.40	1.91	1.33
I	-7.19	25.34	2.02	0.64
J	-2.03	30.50	1.85	0.56
K	1.59	34.11	2.04	0.68
L	63.79	96.32	1.29	-0.28
M	70.77	103.29	1.09	-0.01
N	71.79	104.32	1.05	-0.10

Figures S9, S10, and S11 show all unique structures optimized in the conformational searches, respectively, for SHA, BHA, and SA adsorption onto calcite-[10$\bar{1}$4], with acidic hydrogens included proximal to the ligand adsorbate. Tables S5, S6, and S7 provide corresponding VASPsol- and dipole-corrected DFT-D3 energies of adsorption for each ligand on calcite-[10$\bar{1}$4], given both according to Eq. (S1) and also relative to the lowest energy configuration, species A. Finally, the vertical displacement

(taken along the direction normal to the surface) between the atom in the ligand that is nearest the surface and the highest surface-Ca ion is given as $z_{Ca-SHA/BHA/SA}$, and the height difference between the lowest ligand atom and the highest of all surface atoms is given as $z_{surface-SHA/BHA/SA}$.
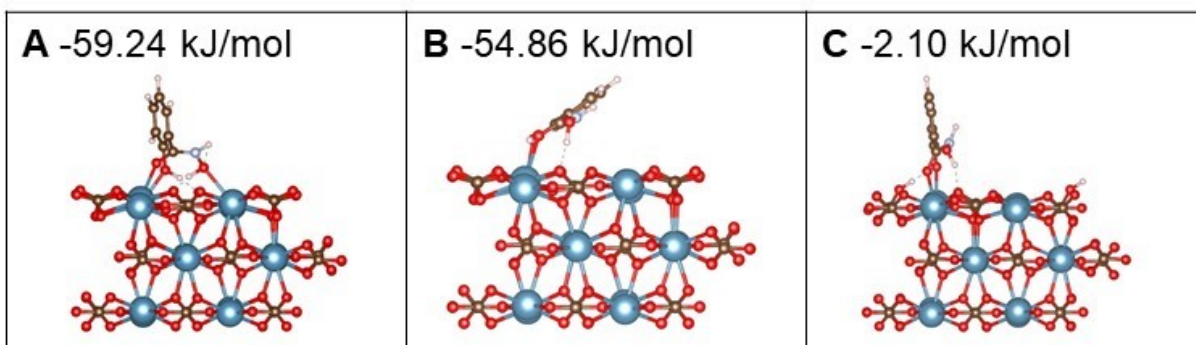
Figure S9. Related to Figure 2 and Table 2: Side views of DFT structures for adsorption of SHA on calcite-[$10\bar{1}4$], including acidic hydrogens. For simplicity, only three layers of the surface slab are shown. Color scheme: Ca: dark blue, C: brown, O: red, N: light blue, H: white. Adsorption energies are also given for each structure. Structures result from conformational search described Transparent Methods section of this file. Species A is that shown in the left panel of Figure 2 of the main text.

Table S5. Related to Figure 2 and Table 2: Energies and interatomic coordinates for SHA adsorbed onto calcite-[$10\bar{1}4$]. Structures result from conformational search described in Transparent Methods section of this file. Species A is that shown in the left panel of Figure 2 of the main text.

| Species	Adsorption Energy / kJ mol^{-1}	Energy Relative to Species A / kJ mol^{-1}	z_{Ca-SHA} / Å	$z_{surf-SHA}$ / Å
A	-59.24	0.00	1.23	0.70
B	-54.86	4.38	1.98	1.46
C	-2.10	57.13	1.86	0.60

Figure S10. Related to Figure 2 and Table 2: Side views of DFT structures for adsorption of BHA on calcite-[10$\bar{1}$4], including acidic hydrogens. For simplicity, only three layers of the surface slab are shown. Color scheme: Ca: dark blue, C: brown, O: red, N: light blue, H: white. Adsorption energies are also given for each structure. Structures result from conformational search described in Transparent Methods section of this file. Species A is that shown in the center panel of Figure 2 of the main text.

Table S6. Related to Figure 2 and Table 2: Energies and interatomic coordinates for BHA adsorbed onto calcite-[10$\bar{1}$4]. Structures result from conformational search described in Transparent Methods section of this file. Species A is that shown in the center panel of Figure 2 of the main text.

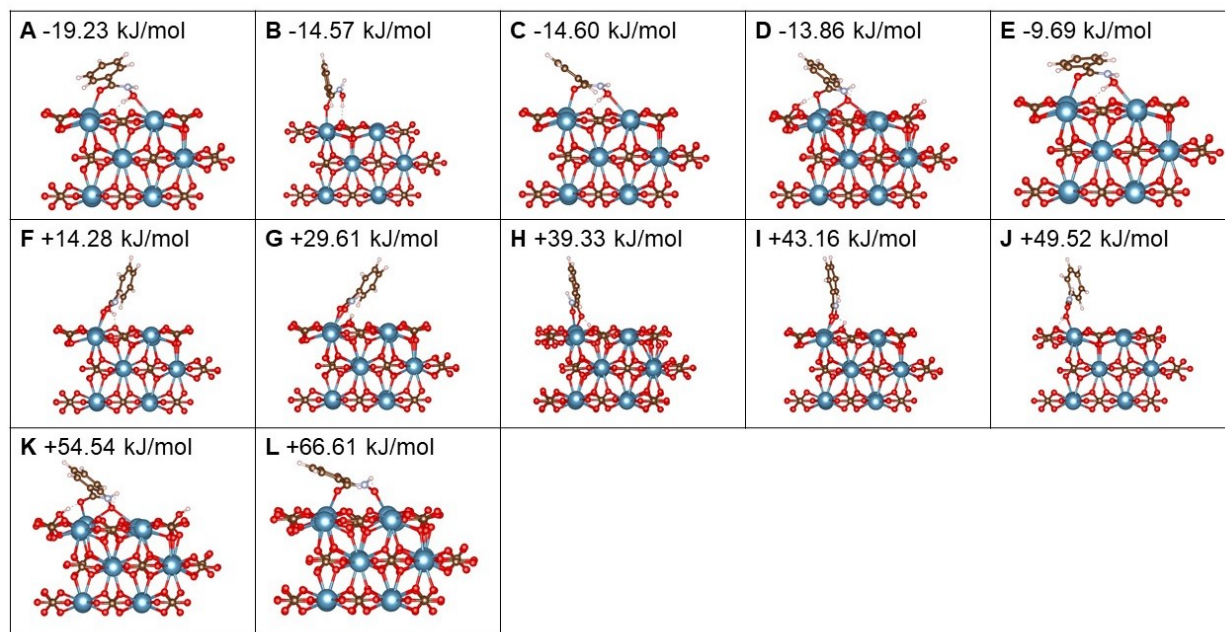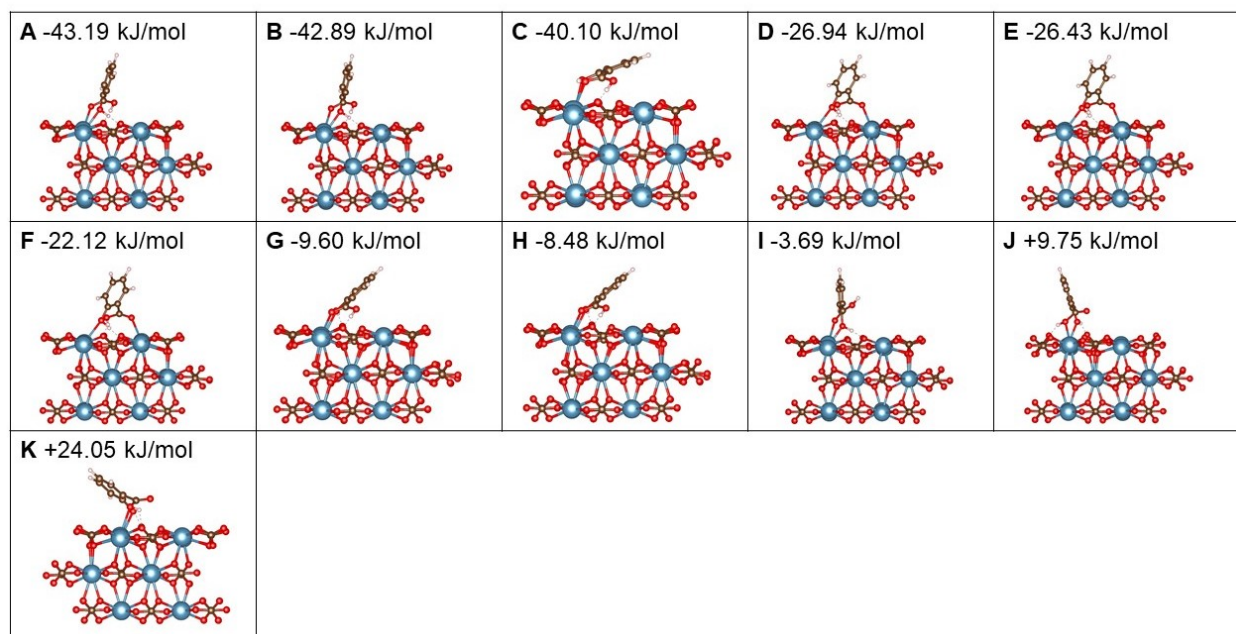| Species	Adsorption Energy / kJ mol^{-1}	Energy Relative to Species A / kJ mol^{-1}	z_{Ca-BHA} / Å	$z_{surf-BHA}$ / Å
A	-19.23	0.00	1.26	0.80
B	-14.57	4.66	2.25	1.48
C	-14.60	4.64	1.35	0.87
D	-13.86	5.38	1.37	0.88
E	-9.69	9.54	1.29	0.83
F	14.28	33.52	1.91	1.24
G	29.61	48.84	1.95	0.59
H	39.33	58.57	1.57	0.81
I	43.16	62.40	1.96	0.58
J	49.52	68.76	1.66	0.95
K	54.54	73.78	1.43	0.07
L	66.61	85.84	1.89	1.44

Figure S11. Related to Figure 2 and Table 2: Side views of DFT structures for adsorption of SA on calcite-[10$\overline{1}$4], including acidic hydrogens. For simplicity, only three layers of the surface slab are shown. Color scheme: Ca: dark blue, C: brown, O: red, N: light blue, H: white. Adsorption energies are also given for each structure. Structures result from conformational search described in Transparent Methods section of this file. Species A is that shown in the right panel of Figure 2 of the main text.

Table S7. Related to Figure 2 and Table 2: Energies and interatomic coordinates for SA adsorbed onto calcite-[10$\overline{1}$4] . Structures result from conformational search described in Transparent Methods section of this file. Species A is that shown in the right panel of Figure 2 of the main text.

Species	Adsorption Energy / kJ mol^{-1}	Energy Relative to Species A / kJ mol^{-1}	z_{Ca-SA} / Å	$z_{surf-SA}$ / Å
A	-43.19	0.00	1.24	0.64
B	-42.89	0.30	1.29	0.67
C	-40.10	3.09	1.56	0.92
D	-26.94	16.25	1.28	0.64
E	-26.43	16.76	1.28	0.64
F	-22.12	21.07	1.23	0.62
G	-9.60	33.59	1.64	0.84
H	-8.48	34.71	1.61	0.82
I	-3.69	39.50	1.24	0.68
J	9.75	52.94	1.82	0.91
K	24.05	67.24	2.03	1.26

Figures S12 and S13 show all unique structures optimized in the conformational searches for the replacement of a surface CO_3^{2-} with doubly deprotonated SHA and SA, respectively, onto bastnäsite-[10$\overline{1}$0]. Tables S8 and S9 provide corresponding VASPsol- and dipole-corrected DFT-D3 energies of replacement for each ligand on bastnäsite-[10$\overline{1}$0], given both according to Eq. (S2) and also relative to the lowest energy configuration, species A. Finally, the vertical displacement (taken along the direction normal to the surface) between the atom in the ligand that is nearest the surface and the highest surface-

Ce ion is given as $z_{Ce-SHA/SA}$, and the height difference between the lowest ligand atom and the highest of all surface atoms is given as $z_{surface-SHA/SA}$.

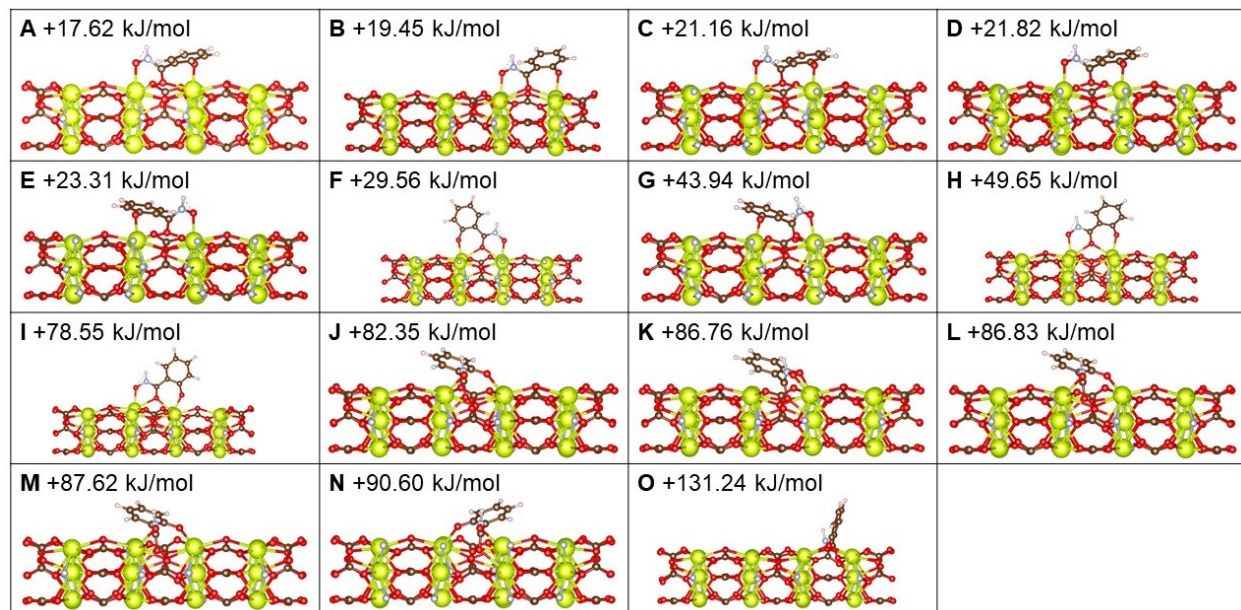**Figure S12. Related to Scheme 1 and Figure 1**: Side views of DFT structures for replacement of a surface CO_3^{2-} with SHA^{2-} on bastnäsite-[$10\bar{1}0$]. For simplicity, only three layers of the surface slab are shown. Color scheme: Ce: green, C: brown, O: red, F/N: light blue. Replacement reaction energies are also given for each structure. Structures result from conformational search described in Transparent Methods section of this file. Species A is that shown in the left panel of Figure S3.

Table S8. Related to Scheme 1 and Figure 1: Energies and interatomic coordinates for replacement of surface CO_3^{2-} in bastnäsite-[$10\bar{1}0$] with SHA^{2-}. Structures result from conformational search described in Transparent Methods section of this file. Species A is that shown in the left panel of Figure S3.

Species	Replacement Energy / kJ mol^{-1}	Energy Relative to Species A / kJ mol^{-1}	z_{Ce-SHA} / Å	$z_{surf-SHA}$ / Å
A	17.62	0.00	0.56	0.10
B	19.45	1.84	0.89	0.48
C	21.16	3.54	0.60	0.12
D	21.82	4.20	0.60	0.12
E	23.31	5.69	0.59	0.11
F	29.56	11.94	1.34	1.05
G	43.94	26.32	0.29	-0.28
H	49.65	32.03	1.32	1.00
I	78.55	60.93	1.20	1.02
J	82.35	64.73	-0.18	-0.83
K	86.76	69.14	-0.29	-0.89
L	86.83	69.21	-0.25	-0.83
M	87.62	70.00	-0.27	-0.85
N	90.60	72.99	-0.33	-0.90
O	131.24	113.62	-0.24	-1.17

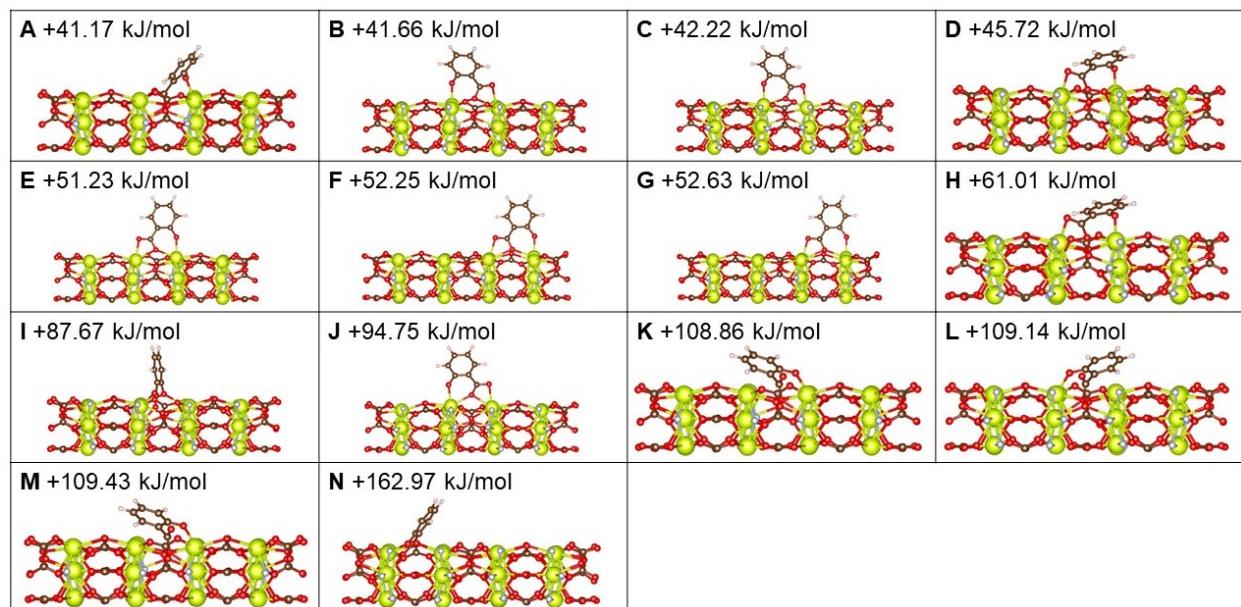| A +41.17 kJ/mol | B +41.66 kJ/mol | C +42.22 kJ/mol | D +45.72 kJ/mol |
E +51.23 kJ/mol	F +52.25 kJ/mol	G +52.63 kJ/mol	H +61.01 kJ/mol
I +87.67 kJ/mol	J +94.75 kJ/mol	K +108.86 kJ/mol	L +109.14 kJ/mol
M +109.43 kJ/mol	N +162.97 kJ/mol		

Figure S13. Related to Scheme 1 and Figure 1: Side views of DFT structures for replacement of a surface CO_3^{2-} with SA^{2-} on bastnäsite-[10$\bar{1}$0]. For simplicity, only three layers of the surface slab are shown. Color scheme: Ce: green, C: brown, O: red, F/N: light blue. Replacement reaction energies are also given for each structure. Structures result from conformational search described in Transparent Methods section of this file. Species A is that shown in the second-from-left panel of Figure S3.

Table S9. Related to Scheme 1 and Figure 1: Energies and interatomic coordinates for replacement of surface CO_3^{2-} in bastnäsite-[10$\bar{1}$0] with SA^{2-}. Structures result from conformational search described in Transparent Methods section of this file. Species A is that shown in the second-from-left panel of Figure S3.

Species	Replacement Energy / kJ mol^{-1}	Energy Relative to Species A / kJ mol^{-1}	z_{Ce-SA} / Å	$z_{surf-SA}$ / Å
A	41.17	0.00	-0.77	-1.31
B	41.66	0.49	0.66	0.32
C	42.22	1.05	0.67	0.33
D	45.72	4.55	0.31	-0.12
E	51.23	10.07	0.87	0.58
F	52.25	11.09	0.82	0.44
G	52.63	11.46	0.44	0.83
H	61.01	19.85	0.26	-0.21
I	87.67	46.50	-0.22	-0.85
J	94.75	53.58	1.15	0.87
K	108.86	67.69	-0.59	-1.15
L	109.14	67.97	-0.57	-1.13
M	109.43	68.26	-0.59	-1.14
N	162.97	121.80	-0.23	-1.00

Figures S14 and S15 show all unique structures optimized in the conformational searches for the replacement of a surface CO_3^{2-} with doubly deprotonated SHA and SA, respectively, onto calcite-[10$\bar{1}$4]. Tables S10 and S11 provide corresponding VASPsol- and dipole-corrected DFT-D3 energies of replacement for each ligand on calcite-[10$\bar{1}$4], given both according to Eq. (S2) and also relative to the

lowest energy configuration, species A. Finally, the vertical displacement (taken along the direction normal to the surface) between the atom in the ligand that is nearest the surface and the highest surface-Ca ion is given as $z_{Ca\text{-}SHA/SA}$, and the height difference between the lowest ligand atom and the highest of all surface atoms is given as $z_{surface\text{-}SHA/SA}$.

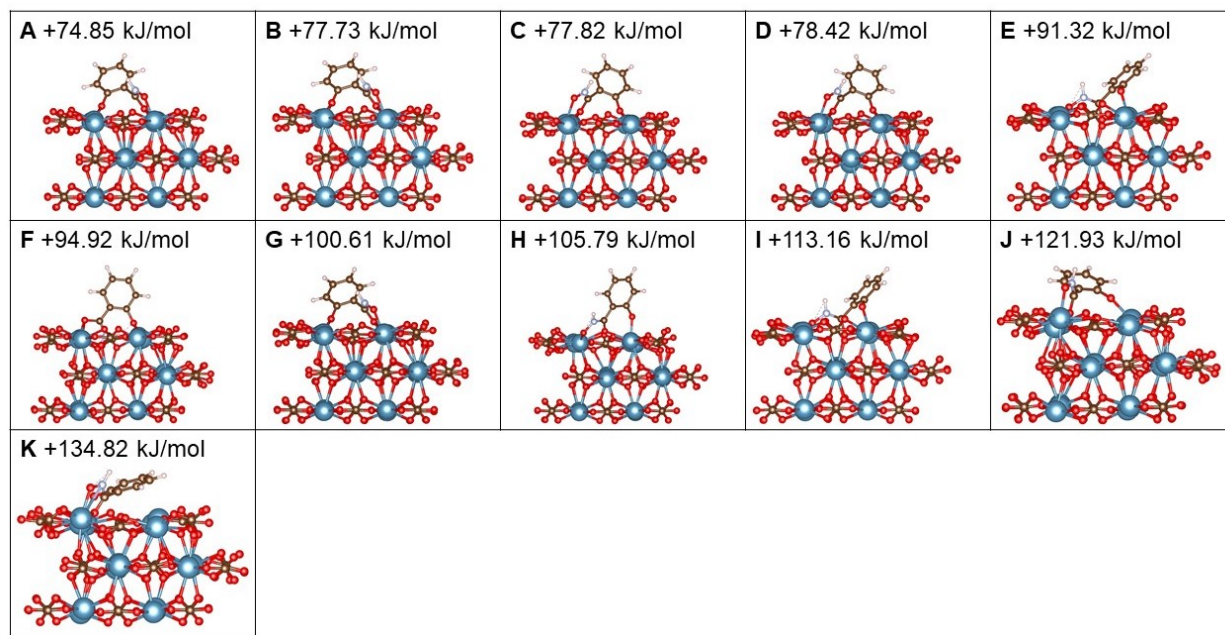| A +74.85 kJ/mol	B +77.73 kJ/mol	C +77.82 kJ/mol	D +78.42 kJ/mol	E +91.32 kJ/mol
F +94.92 kJ/mol	G +100.61 kJ/mol	H +105.79 kJ/mol	I +113.16 kJ/mol	J +121.93 kJ/mol
K +134.82 kJ/mol				

Figure S14. Related to Scheme 1 and Figure 2: Side views of DFT structures for replacement of a surface CO_3^{2-} with SHA^{2-} on calcite-[$10\bar{1}4$]. For simplicity, only three layers of the surface slab are shown. Color scheme: Ce: green, C: brown, O: red, F/N: light blue. Replacement reaction energies are also given for each structure. Structures result from conformational search described in Transparent Methods section of this file. Species A is that shown in the second-from-right panel of Figure S3.

Table S10. Related to Scheme 1 and Figure 2: Energies and interatomic coordinates for replacement of surface CO_3^{2-} in calcite-[$10\bar{1}4$] with SHA^{2-}. Replacement reaction energies are also given for each structure. Structures result from conformational search described in Transparent Methods section of this file. Species A is that shown in the second-from-right panel of Figure S3.

Species	Replacement Energy / kJ mol^{-1}	Energy Relative to Species A / kJ mol^{-1}	$z_{Ca\text{-}SHA}$ / Å	$z_{surf\text{-}SHA}$ / Å
A	74.85	0.00	0.92	0.12
B	77.73	2.88	0.94	0.12
C	77.82	2.97	0.95	0.23
D	78.42	3.57	0.92	0.21
E	91.32	16.47	-0.27	-1.21
F	94.92	20.07	-1.08	-1.68
G	100.61	25.76	0.91	0.11
H	105.79	30.95	0.72	-0.22
I	113.16	38.31	-0.25	-1.22
J	121.93	47.08	0.35	-0.31
K	134.82	59.97	0.38	-0.23

A +78.03 kJ/mol **B** +92.36 kJ/mol **C** +97.26 kJ/mol **D** +97.34 kJ/mol **E** +97.53 kJ/mol

F +98.15 kJ/mol **G** +98.18 kJ/mol **H** +101.01 kJ/mol **I** +101.37 kJ/mol **J** +101.80 kJ/mol

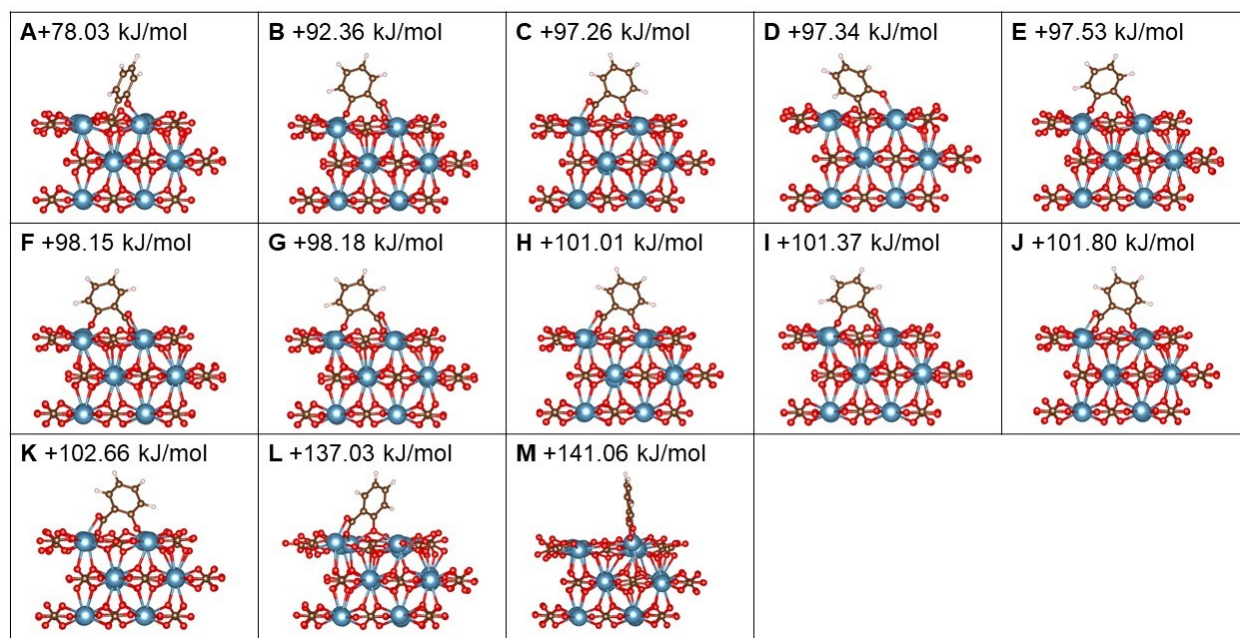**K** +102.66 kJ/mol **L** +137.03 kJ/mol **M** +141.06 kJ/mol

Figure S15. Related to Scheme 1 and Figure 2: Side views of DFT structures for replacement of a surface CO_3^{2-} with SA^{2-} on calcite-[10$\bar{1}$4]. For simplicity, only three layers of the surface slab are shown. Color scheme: Ce: green, C: brown, O: red, F/N: light blue. Replacement reaction energies are also given for each structure. Replacement reaction energies are also given for each structure. Structures result from conformational search described in Transparent Methods section of this file. Species A is that shown in the right panel of Figure S3.

Table S11. Related to Scheme 1 and Figure 2: Energies and interatomic coordinates for replacement of surface CO_3^{2-} in calcite-[10$\bar{1}$4] with SA^{2-}. Structures result from conformational search described in Transparent Methods section of this file. Species A is that shown in the right panel of Figure S3.

Species	Replacement Energy / kJ mol^{-1}	Energy Relative to Species A / kJ mol^{-1}	z_{Ca-SA} / Å	$z_{surf-SA}$ / Å
A	78.03	0.00	-0.55	-1.51
B	92.36	14.33	0.72	-0.04
C	97.26	19.23	0.70	-0.04
D	97.34	19.31	-0.48	-1.45
E	97.53	19.50	0.61	-0.13
F	98.15	20.13	0.61	-0.13
G	98.18	20.15	0.76	-0.03
H	101.01	22.99	0.69	-0.05
I	101.37	23.34	0.69	-0.10
J	101.80	23.77	0.64	-0.05
K	102.66	24.64	0.64	-0.09
L	137.03	59.00	0.69	-0.09
M	141.06	63.03	0.43	-0.04

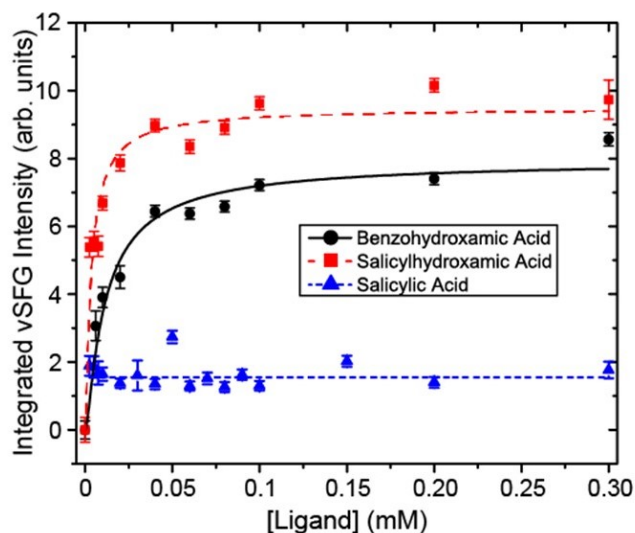*Vibrational Sum Frequency Generation Spectroscopy Data*

Figure S16. Related to Figure 3: Adsorption isotherms for SA (blue), SHA (red), and BHA (black) on bastnäsite-[10$\overline{1}$0] and associated fits, from vSFG data shown in Figure 3b of the main text.

Raman Spectroscopy Data

Figure S17. Related to Figure 5: Raman spectra of aqueous 17-mM SA solution (blue), complex of SA+Ce^{3+} prepared in aqueous solution, pH 8.5 (black), bastnäsite-[10$\overline{1}$0] with 17-mM SA (red), and bastnäsite prior to SA dosing (green). The SA-on-bastnäsite spectrum following subtraction of the bastnäsite spectrum is provided in Figure 5a of the main text.
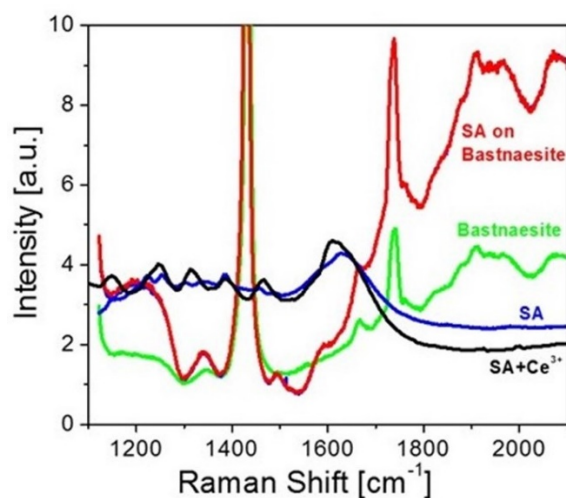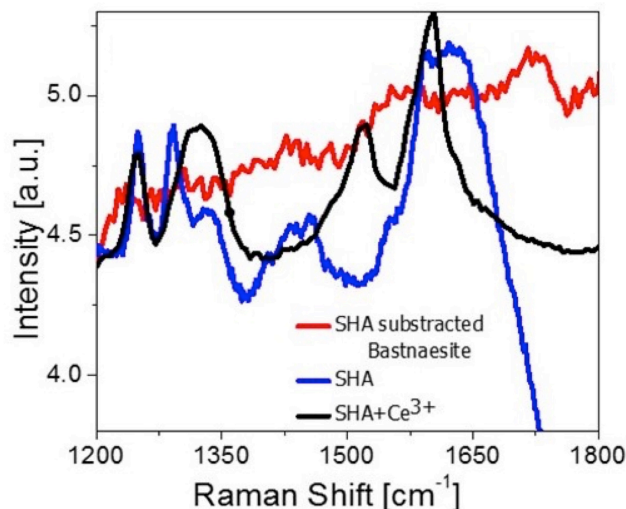
Figure S18. **Related to Figure 5**: Raman spectra of aqueous 17-mM SHA solution (blue), complex of SHA+Ce^{3+} prepared in aqueous solution, pH 8.5 (black), bastnäsite-[10$\bar{1}$0] with 17 mM SHA after the subtraction of the bastnäsite spectrum (red). Figure described in Raman results section of main text.

Transparent Methods

Density Functional Theory

Periodic density-functional-theory calculations were performed using the VASP suite of software (Kresse and Furthmüller, 1996a, b; Kresse and Hafner, 1993, 1994). The valence electronic states were expanded in a basis of plane waves, and the core-valence interactions were described using the projector augmented-wave (PAW) method (Blöchl, 1994; Kresse and Joubert, 1999). A 600-eV cutoff was used, along with the Perdew-Burke-Ernzerhof (PBE) generalized-gradient-approximation (GGA) functional to describe exchange—correlation interactions (Perdew et al., 1996, 1997). Grimme's D3 method was applied throughout (Grimme et al., 2010), to account for van der Waals interactions between adsorbate molecules and surface groups. Cerium was exclusively chosen as the LREE in our DFT calculations for bastnäsite, as Ce is the most abundant LREE found in bastnäsite ores (Eggert et al., 2016). Unpaired electrons in the 4f orbitals of Ce were included in the core when describing the electronic structure of Ce^{3+} ions in bastnäsite. This approximation has been validated previously and shows good agreement with experimental results for bastnäsite lattices (Srinivasan et al., 2016). Surfaces were constructed as 2x2x1 supercells of the most stable surfaces of each mineral, as described previously (Goverapet Srinivasan et al., 2017), resulting in a 7-layer CeFCO$_3$ slab consisting of 336 atoms for bastnäsite-[10$\bar{1}$0], and a 5-layer CaCO$_3$ slab consisting of 200 atoms for calcite-[10$\bar{1}$4]. A 20-Å vacuum layer was added to each surface to prevent interactions of adjacent periodic slab images normal to the surface. Optimization of ligand molecular structures was carried out in an 18 x 18 x 18-Å box.   For all energy calculations, self-consistent-field results were considered converged when the energy calculated from consecutive cycles differed by less than 10^{-5} eV. For geometry optimizations, all atoms were allowed to relax, and geometries were considered relaxed when the force on each atoms was less than 0.01 eV Å^{-1}. The energies of all optimized structures were modified at the single point by a dipole correction normal to the surface (or in all three Cartesian dimensions for species in the absence of mineral surfaces) and by the addition of water solvent, as implemented by the VASPsol implicit solvation model (Fishman et al., 2013; Mathew et al., 2014). The adsorption energy, E$_{ads}$, of a ligand onto a mineral surface was calculated using Eq. (S1):

$$E_{ads} = E_{slab}^{ligand} - E_{slab} - E_{ligand} \quad \text{(S1)}$$

where E_{slab}^{ligand} is the energy of the surface with adsorbed ligand, E_{slab} is the total energy of the surface, and E_{ligand} is the energy of the ligand in the absence of the surface. For each ligand-mineral system, a

conformational search sampling several input geometries for optimization was implemented. The structures and energies of all resulting structures are presented in Figures S6-S11 and Tables S2-S7.

We acknowledge that, at experimental pH ranges, multiple protonation states must be considered, and that ligand deprotonation should occur in solution, prior to adsorption onto the mineral surface. However, constructing such a system in the manner described in this section would require the adsorption of an anionic ligand to a surface without the benefit of charge stabilization by explicit solvent molecules, resulting in an unrealistic description of local surface charge. Thus, we account for deprotonated-ligand adsorption while maintaining charge neutrality within the confines of our model in two ways. First, we constructed multiple protonation states for each adsorbed ligand, allowing for proton donation, when applicable, to a nearby site on the mineral surface. Keeping the proton proximal to the adsorbed hydroxamate/salicylate thereby allows for a molecular approximation of adsorption at elevated pH levels while attempting to maintain a neutral surface charge. Second, for SHA and salicylic acid, which have two acidic protons, charge neutrality was maintained by simply replacing a $CO_3{}^{2-}$ surface dianion with a doubly deprotonated ligand molecule in a separate set of calculations. In this case, reaction energies, E_{rep}, as described in Eq. (S2), for the replacement of a surface carbonate dianion with a di-anionic ligand are considered.

$$E_{rep} = \left(E_{surface}^{doubly\ deprotonated\ ligand} + E_{H_2CO_3} + E_{corr,H_2CO_3}\right) - \left(E_{slab} + E_{ligand} + E_{corr,ligand}\right) \quad \text{(S2)}$$

In Eq. (S2), $E_{surface}^{doubly\ deprotonated\ ligand}$ is the energy of the surface in which a single $CO_3{}^{2-}$ moiety has been replaced with a doubly deprotonated ligand, and E_{slab}, as in Eq. (S1), is the energy of the surface slab prior to the replacement. $E_{H_2CO_3}$ and E_{ligand} are the energies of protonated carbonic acid and ligand molecules. To account for the charge-neutrality using these proton-saturated molecules, an energy correction has been added for both molecules, according to (S3):

$$E_{corr} = 2.303(pH - pK_{a1})RT \qquad \text{(S3)}$$

where E_{corr} is the energy correction (i.e., E_{corr,H_2CO_3} and $E_{corr,ligand}$) in Eq. (S2), pH corresponds to experimental conditions, pK_{a1} is the first acid dissociation constant for the species, R is the ideal gas constant, and T is temperature. For the purposes of this study, T = 298.15 K and pH = 8.5 were used in Eq. (S3). This pH replicates the environment of experiments presented in this work and is in line with conditions of maximum bastnäsite flotation recovery (Fuerstenau, 2013). The pK_a values of the three ligands are provided in Scheme 1 of the main body of text (Humbert et al., 1998; Khalil et al., 2007), and pK_{a1} of H_2CO_3 is 3.6 (Wang et al., 2010). Optimized structures and energies of all species in conformational searches following replacement of $CO_3{}^{2-}$ with di-anionic ligands are provided in Figures S12-S15 and Tables S8-S11.

Collector Ligands

For all experiments, salicylhydroxamic acid (99% purity), salicylic acid, and benzohydroxamic acid (99% purity) were purchased from Millipore Sigma and used as received.

Preparation of Natural Ce-Bastnäsite

Gem-grade bastnäsite from Khyber Pass, Pakistan, was prepared for vSFG and Raman spectroscopy with a Scintillator 88 Gemstone faceting machine. Gems were cleaned and polished along their natural facets using successive grit sandpaper (600 to 1500 grit). The gems were aligned on an x-ray diffractometer (Scintag PDS 2000) equipped with Cu-K_α radiation and a nickel filter. The [10$\overline{1}$0] and the [0001] surfaces were obtained by aligning to the [03$\overline{3}$0] and [0004] Bragg reflections, respectively. These reflections were found at 43.8 and 36.7 degrees 2θ, respectively, and were generally found to be within 5 degrees of the natural facets. After alignment, the gems were polished using successively smaller particle alumina paste (5 to 0.05 μm).

Microflotation

Bastnäsite ore from Mountain Pass, California was used for all microflotation experiments. The ore was sieved to 200x400 mesh (37 – 74 microns) after it was ground for 60 minutes. A Partridge-Smith Cell (Partridge and Smith, 1971) was used for the microflotation experiments. A 52 mL solution was made with 1% ore by weight, collector, sodium carbonate as a pH modifier, and frother. Experiments were conducted at pH 9 and various collector concentrations. The ore was added to distilled water and placed on a stir plate and stirred with a magnetic stir bar at 500 RPM. The collector was dissolved in a small amount of water and was added to the slurry. The pH was adjusted and maintained throughout the 15-minute conditioning stage. One drop of 20 mg/mL methyl isobutyl carbinol frother (Cytec Aerofroth 70) was added to all samples with 2 minutes remaining in the conditioning period. After the conditioning stage, 10 mL of the supernatant was extracted. The remaining slurry was added to the microflotation cell and the beaker was rinsed with the extracted supernatant to prevent material loss. Compressed air was then introduced to the cell at a flow rate of 26.6 cm^3/min. No heat, depressant, or pure minerals were used in microflotation experiments. The concentrates and tailings were both filtered and dried. The experiments were performed in duplicate, and the compositions of the resulting concentrates and tailings were analyzed using X-Ray Fluorescence.

Vibrational Sum Frequency Generation Spectroscopy

Vibrational sum frequency generation (vSFG) is a coherent second-order spectroscopy that is capable of selectively probing interfacial molecular species (Tian and Shen, 2014; Wang, 2016; Wang et al., 2005). Through various experimental designs, researchers are able to use vSFG to quantify interfacial populations and equilibria (Doughty et al., 2016; Voylov et al., 2017), probe molecular ordering (Bordenyuk et al., 2007; Frederick et al., 2011; Jayathilake et al., 2009; Watson et al., 2019), and determine molecular orientations (Doughty et al., 2017; Jang et al., 2013; Liu et al., 2017; Rao et al., 2006; Wanhala et al., 2019) in a range of complex and model systems. In broadband vSFG experiments, two lasers are overlapped in space and in time to drive a coherent second-order polarization in the sample. This polarization oscillates at the sum or difference frequencies between the incident light fields, radiating new light at those frequencies. The measured vSFG intensity is proportional to the mod-square of second-order nonlinear susceptibility, $\chi_{eff}^{(2)}$, of the sample and incident driving laser fields, (E_{IR} and E_{NIR}).

$$I_{\text{vSFG}} \propto |E_{vSFG}|^2 \ \propto \ \left|\chi_{eff}^{(2)} E_{IR} E_{NIR}\right|^2 \tag{S4}$$

The effective second-order nonlinear susceptibility is the sum of resonant, $\chi_{\text{res}}^{(2)}$, and non-resonant, $\chi_{\text{NR}}^{(2)}$, contributions, given by:

$$\chi_{eff}^{(2)} = \chi_{NR}^{(2)} + \chi_{res}^{(2)} = \chi_{NR}^{(2)} + \sum_k \frac{A_k}{\omega_{IR} - \omega_k + i\Gamma_k} \tag{S5}$$

where ω_{IR} are the frequency components of the driving broadband infrared (IR) pulse, A_k is an amplitude that is related to the interfacial population, ω_k is a vibrational resonant frequency, and Γ_k is a linewidth. When frequency components in the broadband IR pulse resonantly excite molecular vibrations in the sample there is an enhancement in the radiated vSFG signal, thereby mapping the vibrational spectrum of the interface.

A detailed description of our second-generation vSFG spectrometer can be found elsewhere (Chowdhury et al., 2018; Chowdhury et al., 2019). Briefly, broadband mid-infrared light (IR) was generated using the output of a regenerative amplifier (Spectra Physics Spitfire Pro) coupled to an optical parametric amplifier (TOPAS-Prime Plus). The IR light was purified with wire grid polarizers and rotated with a zero-order half waveplate before being colinearly combined with spectrally shaped, narrowband near-infrared (NIR) light using a dichroic. The NIR was also polarization-purified and rotated using appropriate optical elements (Chowdhury et al., 2018; Chowdhury et al., 2019). The colinearly propagating beams were focused onto the sample at a 60° angle relative to the surface normal. The radiated vSFG light was collimated with an air-spaced achromatic doublet, polarization resolved, and spectrally filtered before being focused into a spectrograph equipped with a CCD camera.   All spectra were collected in the SSP polarization

combination. vSFG spectra were background-subtracted using neighboring regions of interest to remove the detector offset and residual stray light. These spectra were subsequently scaled by the non-resonant response of the bastnäsite surface itself (Wanhala et al., 2019). Adsorption isotherms were obtained by varying ligand concentrations in solution and measuring the associated vSFG signal. All solutions were pH-adjusted to 8.5 using NaOH immediately before measurements were taken.

The as-purchased ligands were dissolved in ultrapure water (18.2 MΩ·cm) to reach ~1 mM concentration. The resulting solutions were pH adjusted with concentrated NaOH (prepared in ultrapure water) to reach pH ~8.5 as measured using a conventional pH meter and electrode (Thermo Scientific 9157BNMD) immediately before conducting vSFG experiments. The pH-adjusted concentrated stock solutions were diluted into pH ~8.5 ultrapure water to produce sample aliquots used for isotherm measurements. The bastnäsite mineral interface was the same used in other reports (Sutton et al., 2020; Wanhala et al., 2019). The sample was enthusiastically cleaned in between experiments with methanol before being rinsed several times with copious amounts of ultrapure water. Noting that we have observed different spectral features in the present work vs. previous reports (Sutton et al., 2020; Wanhala et al., 2019) studying different ligands at the same mineral sample interface, our results suggest that the mineral interface is free from lingering contaminants and that the vibrations measured in this work originate from the ligands of interest to this work. The vSFG measurements were performed after placing 1-2 drops of solution on the mineral interface and allowing it to incubate for ~2 minutes – the excess solution was wicked away leaving a thin film atop the crystal (Wanhala et al., 2019). The vSFG spectrum was immediately measured to limit evaporation of the remaining water. The isotherms were collected from low to high concentration.

Infrared Spectroscopy

To determine the shift in peak positions with changing protonation state, ATR-FTIR spectra of each ligand in aqueous solution were measured at varying pH, with the bulk water background subtracted. Solutions were measured at concentrations near the limit of solubility of the ligands to enable detection of the ligand (15 mM for SA, 20 mM for BHA and SHA). To help interpret the adsorption mechanism from the FTIR of adsorbed ligands, spectra of cerium complexes were measured directly and compared with those of the uncomplexed ligands. The aqueous complex of each ligand was formed by adding aqueous $CeCl_3$ to the concentrated ligand solution. Spectra of each complex in solution were measured and compared with the pure ligand solution.

ATR-FTIR spectra of each ligand in the adsorbed state were measured *in situ* using a 45° single-reflection diamond/ZnSe internal reflection element (IRE, PIKE Technologies GladiATR). The IRE was coated with a thin film of synthetic Ce-bastnäsite (particle size < 0.5 μm) by adding three 10 μL drops of the solid in methanol suspension (10 g/mL) and allowing the methanol to evaporate.(Shivaramaiah et al., 2016) The dry film was rinsed with DI water, and then a flow cell was added. The particle film was first equilibrated with pH 8.5 NaOH solution (250 mL, recirculating) for 20 minutes, until no further changes were observed in the spectrum. The film in solution was then set as the background before changing the liquid phase to the ligand solution. Spectra were measured at 20-minute intervals as the ligand adsorbed, for a total of 60 minutes. The solutions used for adsorption experiments (0.5-2 mM) were below the detection limit of the ligands in solution; thus, peaks corresponding to the ligand appeared as a result of adsorption onto the bastnäsite film.

Raman Spectroscopy

Raman spectra were obtained using a XploRA spectrometer (Horiba) coupled with an Olympus microscope equipped with a 10x (0.25 NA) objective. The spectrometer was set with a 300-μm pinhole, and the diffraction grating for Raman measurements was set to an 1800-gr/mm. Spectra were obtained using a 532 nm laser.

Solutions of ~17 mM and ~2 mM SHA, ~17 mM SA, and ~18 mM BHA were dissolved in water, adjusted to pH 8.5 using NaOH, and used in studies with bastnäsite. Separately, aqueous complexes of collectors with Ce^{3+} ions were prepared by mixing 16-mM solutions of collectors with 16 mM $CeCl_3$ in water at pH

8.5. Raman spectra of these solutions were acquired by placing 2-3 mL of the solution onto a glass microscope slide with a single cavity well, while for experiments on the bastnäsite crystals, a small drop was placed on the surface of the crystal, and spectra were measured after 50 min.

Supplemental References

Blöchl, P.E. (1994). Projector augmented-wave method. Physical Review B *50*, 17953-17979.

Bordenyuk, A.N., Weeraman, C., Yatawara, A., Jayathilake, H.D., Stiopkin, I., Liu, Y., and Benderskii, A.V. (2007). Vibrational Sum Frequency Generation Spectroscopy of Dodecanethiol on Metal Nanoparticles. The Journal of Physical Chemistry C *111*, 8925-8933.

Chowdhury, A.U., Liu, F., Watson, B.R., Ashkar, R., Katsaras, J., Patrick Collier, C., Lutterman, D.A., Ma, Y.-Z., Calhoun, T.R., and Doughty, B. (2018). Flexible approach to vibrational sum-frequency generation using shaped near-infrared light. Optics Letters *43*, 2038-2041.

Chowdhury, A.U., Watson, B.R., Ma, Y.-Z., Sacci, R.L., Lutterman, D.A., Calhoun, T.R., and Doughty, B. (2019). A new approach to vibrational sum frequency generation spectroscopy using near infrared pulse shaping. Review of Scientific Instruments *90*, 033106.

Doughty, B., Goverapet Srinivasan, S., Bryantsev, V.S., Lee, D., Lee, H.N., Ma, Y.-Z., and Lutterman, D.A. (2017). Absolute Molecular Orientation of Isopropanol at Ceria (100) Surfaces: Insight into Catalytic Selectivity from the Interfacial Structure. The Journal of Physical Chemistry C *121*, 14137-14146.

Doughty, B., Yin, P., and Ma, Y.-Z. (2016). Adsorption, Ordering, and Local Environments of Surfactant-Encapsulated Polyoxometalate Ions Probed at the Air–Water Interface. Langmuir *32*, 8116-8122.

Eggert, R., Wadia, C., Anderson, C., Bauer, D., Fields, F., Meinert, L., and Taylor, P. (2016). Rare Earths: Market Disruption, Innovation, and Global Supply Chains. Annual Review of Environment and Resources *41*, 199-222.

Fishman, M., Zhuang, H.L., Mathew, K., Dirschka, W., and Hennig, R.G. (2013). Accuracy of exchange-correlation functionals and effect of solvation on the surface energy of copper. Physical Review B *87*, 245402.

Frederick, M.T., Achtyl, J.L., Knowles, K.E., Weiss, E.A., and Geiger, F.M. (2011). Surface-Amplified Ligand Disorder in CdSe Quantum Dots Determined by Electron and Coherent Vibrational Spectroscopies. Journal of the American Chemical Society *133*, 7476-7481.

Fuerstenau, D.W. (2013). Design and development of novel flotation reagents for the beneficiation of Mountain Pass rare-earth ore. Minerals & Metallurgical Processing *30*, 1-9.

Goverapet Srinivasan, S., Shivaramaiah, R., Kent, P.R.C., Stack, A.G., Riman, R., Anderko, A., Navrotsky, A., and Bryantsev, V.S. (2017). A comparative study of surface energies and water adsorption on Ce-bastnäsite, La-bastnäsite, and calcite via density functional theory and water adsorption calorimetry. Physical Chemistry Chemical Physics *19*, 7820-7832.

Grimme, S., Antony, J., Ehrlich, S., and Krieg, H. (2010). A consistent and accurate ab initio parametrization of density functional dispersion correction (DFT-D) for the 94 elements H-Pu. The Journal of Chemical Physics *132*, 154104.

Humbert, B., Alnot, M., and Quilès, F. (1998). Infrared and Raman spectroscopical studies of salicylic and salicylate derivatives in aqueous solution. Spectrochimica Acta Part A: Molecular and Biomolecular Spectroscopy *54*, 465-476.

Jang, J.H., Lydiatt, F., Lindsay, R., and Baldelli, S. (2013). Quantitative Orientation Analysis by Sum Frequency Generation in the Presence of Near-Resonant Background Signal: Acetonitrile on Rutile TiO2 (110). The Journal of Physical Chemistry A *117*, 6288-6302.

Jayathilake, H.D., Driscoll, J.A., Bordenyuk, A.N., Wu, L., da Rocha, S.R.P., Verani, C.N., and Benderskii, A.V. (2009). Molecular Order in Langmuir−Blodgett Monolayers of Metal−Ligand Surfactants Probed by Sum Frequency Generation. Langmuir *25*, 6880-6886.

Khalil, M.M., El-Deeb, M.M., and Mahmoud, R.K. (2007). Equilibrium Studies of Binary Systems Involving Lanthanide and Actinide Metal Ions and Some Selected Aliphatic and Aromatic Monohydroxamic Acids. Journal of Chemical & Engineering Data *52*, 1571-1579.

Kresse, G., and Furthmüller, J. (1996a). Efficiency of ab-initio total energy calculations for metals and semiconductors using a plane-wave basis set. Computational Materials Science *6*, 15-50.

Kresse, G., and Furthmüller, J. (1996b). Efficient iterative schemes for ab initio total-energy calculations using a plane-wave basis set. Physical Review B *54*, 11169-11186.

Kresse, G., and Hafner, J. (1993). Ab initio molecular dynamics for liquid metals. Physical Review B *47*, 558-561.

Kresse, G., and Hafner, J. (1994). Ab initio molecular-dynamics simulation of the liquid-metal--amorphous-semiconductor transition in germanium. Physical Review B *49*, 14251-14269.

Kresse, G., and Joubert, D. (1999). From ultrasoft pseudopotentials to the projector augmented-wave method. Physical Review B *59*, 1758-1775.

Liu, W., Wang, X., Xu, H., and Miller, J.D. (2017). Physical chemistry considerations in the selective flotation of bastnaesite with lauryl phosphate. Minerals & Metallurgical Processing *34*, 116-124.

Mathew, K., Sundararaman, R., Letchworth-Weaver, K., Arias, T.A., and Hennig, R.G. (2014). Implicit solvation model for density-functional study of nanocrystal surfaces and reaction pathways. The Journal of Chemical Physics *140*, 084106.

Partridge, A., and Smith, G. (1971). Small-sample flotation testing: a new cell. Trans Inst Min Metall, Sect C *80*, 118.

Perdew, J.P., Burke, K., and Ernzerhof, M. (1996). Generalized Gradient Approximation Made Simple. Physical Review Letters *77*, 3865-3868.

Perdew, J.P., Burke, K., and Ernzerhof, M. (1997). Generalized Gradient Approximation Made Simple [Phys. Rev. Lett. 77, 3865 (1996)]. Physical Review Letters *78*, 1396-1396.

Rao, Y., Comstock, M., and Eisenthal, K.B. (2006). Absolute Orientation of Molecules at Interfaces. The Journal of Physical Chemistry B *110*, 1727-1732.

Shivaramaiah, R., Anderko, A., Riman, R.E., and Navrotsky, A. (2016). Thermodynamics of bastnaesite: A major rare earth ore mineral. American Mineralogist *101*, 1129-1134.

Srinivasan, S.G., Shivaramaiah, R., Kent, P.R.C., Stack, A.G., Navrotsky, A., Riman, R., Anderko, A., and Bryantsev, V.S. (2016). Crystal Structures, Surface Stability, and Water Adsorption Energies of La-Bastnäsite via Density Functional Theory and Experimental Studies. The Journal of Physical Chemistry C *120*, 16767-16781.

Sutton, J.E., Roy, S., Chowdhury, A.U., Wu, L., Wanhala, A.K., De Silva, N., Jansone-Popova, S., Hay, B.P., Cheshire, M.C., Windus, T.L.*, et al.* (2020). Molecular Recognition at Mineral Interfaces: Implications for the Beneficiation of Rare Earth Ores. ACS Applied Materials & Interfaces.

Tian, C.S., and Shen, Y.R. (2014). Recent progress on sum-frequency spectroscopy. Surface Science Reports *69*, 105-131.

Voylov, D.N., Holt, A.P., Doughty, B., Bocharova, V., Meyer, H.M., Cheng, S., Martin, H., Dadmun, M., Kisliuk, A., and Sokolov, A.P. (2017). Unraveling the Molecular Weight Dependence of Interfacial Interactions in Poly(2-vinylpyridine)/Silica Nanocomposites. ACS Macro Letters *6*, 68-72.

Wang, H.-F. (2016). Sum frequency generation vibrational spectroscopy (SFG-VS) for complex molecular surfaces and interfaces: Spectral lineshape measurement and analysis plus some controversial issues. Progress in Surface Science *91*, 155-182.

Wang, H.-F., Gan, W., Lu, R., Rao, Y., and Wu, B.-H. (2005). Quantitative spectral and orientational analysis in surface sum frequency generation vibrational spectroscopy (SFG-VS). International Reviews in Physical Chemistry *24*, 191-256.

Wang, X., Conway, W., Burns, R., McCann, N., and Maeder, M. (2010). Comprehensive Study of the Hydration and Dehydration Reactions of Carbon Dioxide in Aqueous Solution. The Journal of Physical Chemistry A *114*, 1734-1740.

Wanhala, A.K., Doughty, B., Bryantsev, V.S., Wu, L., Mahurin, S.M., Jansone-Popova, S., Cheshire, M.C., Navrotsky, A., and Stack, A.G. (2019). Adsorption mechanism of alkyl hydroxamic acid onto bastnäsite: Fundamental steps toward rational collector design for rare earth elements. Journal of Colloid and Interface Science *553*, 210-219.

Watson, B.R., Ma, Y.-Z., Cahill, J.F., Doughty, B., and Calhoun, T.R. (2019). Probing ligand removal and ordering at quantum dot surfaces using vibrational sum frequency generation spectroscopy. Journal of Colloid and Interface Science *537*, 389-395.